Master Thesis

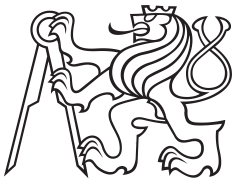

Czech Technical University in Prague

F3

Faculty of Electrical Engineering
Department of Control Engineering

Robust attitude control of cubesat spacecraft

Bc. Dominik Beňo

Supervisor: Doc. Ing. Martin Hromčík, Ph.D.
Field of study: Cybernetics and Robotics
May 2024

MASTER‘S THESIS ASSIGNMENT

I. Personal and study details

Student's name: **Beňo Dominik** Personal ID number: **492051**

Faculty / Institute: **Faculty of Electrical Engineering**

Department / Institute: **Department of Control Engineering**

Study program: **Cybernetics and Robotics**

II. Master’s thesis details

Master’s thesis title in English:

Robust attitude control of cubesat spacecraft

Master’s thesis title in Czech:

Robustní řízení orientace cubesat-satelitu

Guidelines:

The goal of the thesis is to design an attitude controller for a spacecraft of 6U Cubesat class ambitious mission. The spacecraft mission demands high pointing performance, agility and stability which pose stringent controller performance requirements. The spacecraft is designed by following the new-space approach with components available commercially off-the-shelf, resulting in dynamics with significant parametric uncertainties. There are also significant disturbances originating in the environment and in the spacecraft due to moving/rotating parts and appendages. The proposed controller shall take all modeled disturbances and uncertainties into consideration, and it shall be validated in high-fidelity simulation software.

1. Develop a control-oriented mathematical model of the Cubesat spacecraft attitude dynamics including appendages and external/internal disturbances.
2. Build a simulation model using an available attitude simulator and compare the proposed models with simulated responses.
3. Design and implement robust controllers satisfying performance, agility and robustness requirements considering identified uncertainties and disturbances.
4. Validate the controller in closed-loop simulation and discuss the benefits of the proposed approach over the single-axis control.

Bibliography / sources:

[1] Markley, F. Landis, and John L. Crassidis. Fundamentals of spacecraft attitude determination and control. Vol. 1286. New York, NY: Springer New York, 2014.
[2] Stoneking, Eric, 42: A General-Purpose Spacecraft Simulation, NASA Software Designation GSC-16720-1, 2010-2019. https://sourceforge.net/projects/fortytwospacecraftsimulation, https://github.com/ericstoneking/42.
[3] Skogestad, Sigurd, and Ian Postlethwaite. Multivariable feedback control: analysis and design. john Wiley & sons, 2005.

Name and workplace of master’s thesis supervisor:

doc. Ing. Martin Hromčík, Ph.D. Department of Control Engineering FEE

Name and workplace of second master’s thesis supervisor or consultant:

Date of master’s thesis assignment: **22.01.2024** Deadline for master's thesis submission: **24.05.2024**

Assignment valid until:
by the end of summer semester 2024/2025

doc. Ing. Martin Hromčík, Ph.D.	prof. Ing. Michael Šebek, DrSc.	prof. Mgr. Petr Páta, Ph.D.
Supervisor’s signature	Head of department’s signature	Dean’s signature

III. Assignment receipt

The student acknowledges that the master's thesis is an individual work. The student must produce his thesis without the assistance of others, with the exception of provided consultations. Within the master's thesis, the author must state the names of consultants and include a list of references.

.	
Date of assignment receipt	Student's signature

Acknowledgements

I would like to thank my thesis supervisor Martin Hromčík for his thoughtful guidance during the development of this thesis. He gave me valuable feedback always when I needed.

I would like to thank Dávid and Juraj for helping me getting into AOCS problematic and for their professional and technical help with spacecraft control problematic.

My gratitude belongs to Simonka and my family for their patience and support throughout all my studies.

Last but not least, I would also like to thank all teachers for providing me with the theoretical knowledge necessary for the creation of this thesis.

Declaration

I declare that the presented work was developed independently and that I have listed all sources of information used within it in accordance with the methodical instructions for observing the ethical principles in the preparation of university theses.

In Prague, 24. May 2024

.....

Bc. Dominik Beňo

Abstract

This thesis presents a study on the robust attitude control of a 6U CubeSat satellite. The research focuses on the development and implementation of control laws to meet the stringent mission requirements for precise satellite attitude control. Two control-oriented models are developed: one considering the satellite as a rigid body, and the other incorporating flexible solar panels. These models are utilized to design and analyze controllers using LQR optimal control problem and signal-based H_∞ control method. The controllers are evaluated in software in the loop simulations, including Monte Carlo analysis, to assess their properties under parametric uncertainties.

Keywords: CubeSat, satellite attitude control, Monte Carlo simulations, mission requirements, linear control, stability analysis

Supervisor: Doc. Ing. Martin Hromčík, Ph.D.

Abstrakt

Tato práce představuje studii robustního řízení orientace družice 6U CubeSat satelitu. Práce se zaměřuje na vývoj a implementaci řídicích zákonů, které splňují přísné požadavky mise na přesné řízení orientace družice. Byly vyvinuty dva modely orientované na řízení: jeden uvažuje družici jako tuhé těleso a druhý zahrnuje ohebné solární panely. Tyto modely byly použity k návrhu a analýze regulátorů pomocí problému optimálního řízení LQR a metody řízení H_∞ založené na penalizaci signálu. Regulátory byly ověřeny v simulacích uzavřené smyčky SIL včetně analýzy Monte Carlo k posouzení jejich výkonnosti při parametrických neurčitostech.

Klíčová slova: CubeSat, řízení orientace satelitu, Monte Carlo simulace, požadavky mise, lineární řízení, analýza stability

Překlad názvu: Robustní řízení orientace cubesat-satelitu

Contents

Figures

Tables

Chapter 1

Introduction

CubeSats are a class of miniaturized satellites, that have revolutionized space technology by offering high-tech capabilities at a fraction of the cost of traditional satellites. Their small size and modular design enable a wide range of missions, from scientific research to Earth observation. From a scientific point of view it is good to mention a successful NASA JPL ASTERIA mission, which utilized 6U CubeSat with very precise attitude control as a demonstrator to conduct precise astrophysical measurements using a CubeSat [4]. The first Czech CubeSat VZLUSAT-1 was launched in 2017, which was the world's second longest operating 2U satellite [5]. Since then multiple Czech and Slovak Cubesats conducting science, Earth observation, or serving as a technology demonstration, were launched. The Czech space industry grows fast and in a few years Czech Republic will have the first Czech space telescope QUVIK in orbit gathering science data[6].

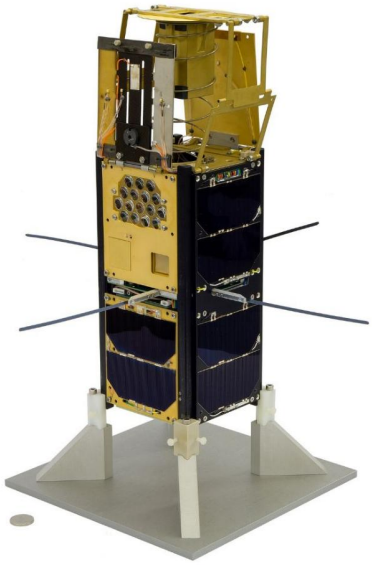

(a) : VZLUSAT-1 CubeSat [5]

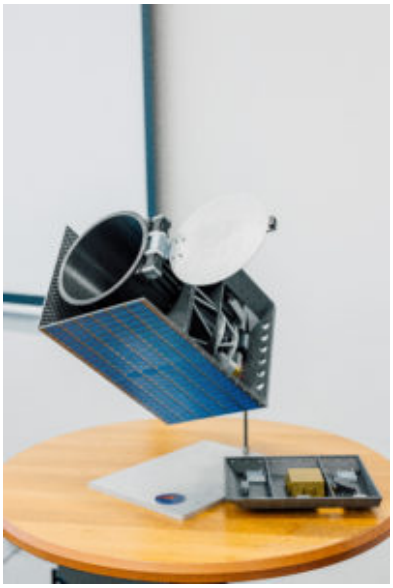

(b) : Miniaturized model of QUVIK telescope [6]

Figure 1.1: Czech satellites

This thesis is about the design of robust attitude control for the 6U CubeSat platform. As will be shown in the thesis CubeSat is very complex, in order to fulfill all its tasks to satisfy the mission requirements given on the attitude control subsystem. In this thesis, the effect of environment disturbances and measurement noise affecting fine pointing and object tracking scenarios will be studied. Furthermore, the thesis aims to support the future Czech space missions by its outcomes.

To fulfill this goal, thesis is outlined into several parts. In the first part, a dynamical model of a satellite will be developed and verified in high-fidelity simulation. Other subsystems related to the attitude control will be described. Disturbance torques affecting the satellite will be analyzed and modeled. In the second part, several controllers will be designed using different approaches, analyzed, and compared. The last part of the thesis will be designated to the validation of the controllers in the closed-loop simulation using high-fidelity simulator in software in the loop(SIL) simulation.

1.1 Thesis goals

The main goals of this thesis are summarized below:

- Development of a control-oriented model of satellite with appendages.
- Analysis and modeling of external/internal disturbances affecting the system.
- Validation of control-oriented model with high-fidelity simulator.
- Design of controllers satisfying ECSS and mission requirements.
- Validation of designed controllers using high-fidelity simulator.

Part I

Satellite model

Chapter 2

Satellite attitude dynamical model

2.1 Reference frames

For satellite attitude control, various reference frames could be used. In this chapter the frames used in the thesis are discussed. The picture of satellite with coordinate systems is in the figure 3.1.

2.1.1 Spacecraft body frame

The body coordinate system is linked to the spacecraft and is defined directly on the body of the spacecraft. Its origin is located at the center of the mass of the spacecraft. There may be different ways to define its axes.

The spacecraft body axes from this thesis are aligned in the following order: Body axis $\boldsymbol{b_1}$ or x-axis corresponds to the spacecrafts camera axis. The axis parallel to the solar panels attachment is marked as $\boldsymbol{b_3}$ or z-axis. The remaining third axis $\boldsymbol{b_2}$, y-axis, is aligned such that the cross product of unit vectors holds relation $\boldsymbol{b_3} = \boldsymbol{b_1} \times \boldsymbol{b_2}$.

2.1.2 Inertial frame

The Earth-centred inertial (ECI) frame of reference is very useful for describing satellite dynamics and kinematics. On the one hand, an inertial frame is a frame in which Newton's laws of motion and gravity are valid. On the other hand, many spacecraft are inertial pointing spacecraft.

The frame is defined relative to the Earth's rotation axis and the ecliptic plane. The Earth's equator plane and ecliptic have two intersections. The ECI frame is defined at one of these equinoxes, the vernal equinox. This can happen multiple times, so the orientation of the axes is from the 01.01.2000 12:00 TDB. So the frame is also called J2000. The x-axis $\boldsymbol{n_1}$ is the direction from the Earth center to the vernal equinox. The z-axis $\boldsymbol{n_3}$ is the rotation axis of the Earth. The y-axis $\boldsymbol{n_2}$ follows the right-hand rule $\boldsymbol{n_3} = \boldsymbol{n_1} \times \boldsymbol{n_2}$ [7].

2.1.3 Orbital frame(LVLH)

Orbital frame or local vertical local horizontal frame (LVLH) is very useful for Earth pointing satellites. The origin of the frame is the center of mass of the spacecraft.

The z-axis $\boldsymbol{l_3}$ is always pointing to the center of the Earth(nadir pointing). The x-axis $\boldsymbol{l_1}$ is perpendicular to $\boldsymbol{l_3}$ and its direction is along the spacecraft velocity direction. The y-axis $\boldsymbol{l_2}$ follows the right-hand rule $\boldsymbol{l_3} = \boldsymbol{l_1} \times \boldsymbol{l_2}$ [7].

2.2 Attitude dynamics

For modeling satellite dynamics, I model the satellite as a rigid body and express equations in a body coordinate system. Let $\boldsymbol{J}_B$ be the moment of inertia matrix of the satellite. Rotational dynamics of the satellite has three states corresponding to the angular velocity vector of the satellite body with respect to the inertial frame in the satellite body frame $\boldsymbol{\omega}_I$. Let $\boldsymbol{h}_I$ be the angular momentum vector of the satellite about its center of mass represented in the inertial frame and $\boldsymbol{h} = \boldsymbol{J}_B \boldsymbol{\omega}_I$ the same angular momentum vector expressed in the body frame [7]. From the law of conservation of angular momentum, its derivative can be expressed as

$$\dot{\boldsymbol{h}}_{\mathrm{I}} = \boldsymbol{L}_{\mathrm{ext}} \tag{2.1}$$

where $\boldsymbol{L}_{\mathrm{ext}}$ is external torque acting on the body. Furthermore

$$\dot{\boldsymbol{h}}_I = \dot{\boldsymbol{h}} + \boldsymbol{\omega}_I \times \boldsymbol{h} \tag{2.2}$$

Substituting equation 2.2 into the equation 2.1 an Euler's rotational equation is obtained

$$\boldsymbol{J}_B \dot{\boldsymbol{\omega}}_I = \boldsymbol{L}_{\mathrm{ext}} - \boldsymbol{\omega}_I \times \boldsymbol{h} \tag{2.3}$$

describing the rotational dynamics of the satellite. External torque vector consists of the control input torques $\boldsymbol{u}$ and disturbance torques $\boldsymbol{d}$, due to gravitational, aerodynamic, and other environmental torques.

2.3 Attitude kinematics

The attitude of the satellite can be described by multiple representations of the rotation such as Euler angles, rotation matrix, quaternions, Rodriguez parameters, etc.[1]. In this thesis attitude kinematics is represented by quaternions.

The main reason for this type of attitude representation is that quaternions do not have singularities like Euler angles [7]. Denote the rotational axis of a body frame relative to the reference frame by a unit length vector $\boldsymbol{e}$ and the

rotational angle α around the rotational axis. Quaternion $\boldsymbol{q}$ representing the rotation around $\boldsymbol{e}$ by angle α is a tuple of four real numbers.

$$\boldsymbol{q} = \begin{pmatrix} \cos\left(\frac{\alpha}{2}\right) \\ \boldsymbol{e}\sin\left(\frac{\alpha}{2}\right) \end{pmatrix} = \begin{pmatrix} q_0 & q_1 & q_2 & q_3 \end{pmatrix}^T \tag{2.4}$$

Assume that satellite rotates with angular velocity $\boldsymbol{\omega}$ with respect to reference frame. The satellite's orientation with respect to the reference frame is expressed by quaternion $\boldsymbol{q}$. The equation 2.5 represents the nonlinear kinematics[7].

$$\dot{\boldsymbol{q}} = \frac{1}{2}\begin{pmatrix} q_0 & -q_1 & -q_2 & -q_3 \\ q_1 & q_0 & -q_3 & q_2 \\ q_2 & q_3 & q_0 & -q_1 \\ q_3 & -q_2 & q_1 & q_0 \end{pmatrix}\begin{pmatrix} 0 \\ \boldsymbol{\omega} \end{pmatrix} \tag{2.5}$$

The state space model of satellite attitude dynamics and kinematics is expressed by equations 2.3 and 2.5. The system model has seven states and is uncontrollable after linearization [7]. The dimension of the system can be reduced using reduced quaternion kinematics. The q_0 can be expressed by the following relation:

$$q_0(q_1,\, q_2,\, q_3) = \sqrt{1 - q_1^2 - q_2^2 - q_3^2} \tag{2.6}$$

By substituting equation 2.6 into equation 2.5 the reduced quaternion kinematics can be obtained in the equation 2.7.

$$\dot{\boldsymbol{q}} = \frac{1}{2}\boldsymbol{Q}(q_1, q_2, q_3)\boldsymbol{\omega} = \frac{1}{2}\begin{pmatrix} q_0(q_1, q_2, q_3) & -q_3 & q_2 \\ q_3 & q_0(q_1, q_2, q_3) & -q_1 \\ -q_2 & q_1 & q_0(q_1, q_2, q_3) \end{pmatrix}\boldsymbol{\omega} \tag{2.7}$$

The reduced quaternion kinematics has an advantage in the smaller system order. Additionally, the system consisting of the satellite attitude dynamics 2.3 and reduced quaternion kinematics 2.7 is controllable when linearized. By expressing q_0 a singularity at $\alpha = \pm\pi$ in the reduced attitude kinematics is introduced [7].

2.4 Disturbances

As was mentioned in the section 2.2 satellite is affected by disturbances, which affect the attitude of the satellite. Disturbances create a torque acting on the satellite body. There are several disturbance torques induced by the space environment. Some of the sources of the disturbance errors can be incorporated into the satellite model using simplifications, but mostly the environmental torques are difficult to model and introduce uncertainties.

Some disturbance torques come from the structure of the satellite such as deployable solar panels, booms, rotating parts, or spinning reaction wheels [1].

2.4.1 External torques

External torques change the overall momentum of the spacecraft. These sources of torques come mostly from the space environment. If an information regarding the geometry of the spacecraft, electrical and mechanical properties of spacecraft, and knowledge of attitude, angular velocity, position and velocity of spacecraft, etc. is available, then these disturbances can be modeled and used for compensation in feedforward. Some of these environmental torques can be modeled as a function of spacecraft attitude and angular velocity and can be embedded in the system model. Usually, the designed controller performance should be verified in simulation, which includes the space environment model and disturbance torques omitted in the controller design [7].

Gravity gradient torque

If an asymmetrical rigid body is placed into the gravity field, it is subjected to gravity gradient torque. This torque can be computed by summing torque contributions of the gravitational forces on the point masses constituting the rigid body.

$$\boldsymbol{F}^i_{\text{ext}} = -m_i \frac{\mu \boldsymbol{r}^i}{\|\boldsymbol{r}^i\|^3} \tag{2.8}$$

Where μ is a gravitational constant, m_i is the mass of point mass and $\boldsymbol{r}^i$ is the vector from the center of mass of the Earth to the point mass.

With knowledge of attitude quaternion between body frame and LVLH frame $\boldsymbol{q}_\text{l}$, orbit rate ω_o and satellite moment of inertia $\boldsymbol{J}_B$ the resulting nonlinear relation for gravity gradient torque can be expressed[7]:

$$\boldsymbol{L}_{gg} = 3\,\omega_0^2\,\boldsymbol{R}(\boldsymbol{q}_\text{l}) \times (\boldsymbol{J}_B \boldsymbol{R}(\boldsymbol{q}_\text{l})) \tag{2.9}$$

$\boldsymbol{R}(\boldsymbol{q}_\text{l})$ is a vector from the center of Earth to the center of mass of the spacecraft represented in the body frame.

Gravity gradient can be stabilizing or destabilizing. It depends on the mass distribution of the rigid body. As can be seen in the equation 2.10, in which nonlinear relation for $\boldsymbol{L}_{gg}$ is linearized around $\boldsymbol{q}_l = (1, 0, 0, 0)$ and diagonal $\boldsymbol{J}_B = \text{diag}(J_{11}, J_{22}, J_{33})$ is assumed. It can be seen that $\boldsymbol{q}_l$ is stable equilibrium if J_{33} is the smallest element of the $\boldsymbol{J}_B$ matrix [1].

$$\boldsymbol{L}_{gg} = \begin{pmatrix} 6\omega_0^2(J_{33} - J_{22})q_{l1} \\ 6\omega_0^2(J_{33} - J_{11})q_{l2} \\ 0 \end{pmatrix} \tag{2.10}$$

Aerodynamic torque

The atmosphere in low Earth orbits causes one of the major disturbance torques for spacecraft. For modeling the aerodynamic torque, the knowledge

of spacecraft geometry is needed. Each part of the satellite can be exposed to the air with a different area S_i, depending on the attitude of the spacecraft. Furthermore, the air density ρ is not constant and is dependent on several factors such as the altitude, temperature of the spacecraft, and composition of the upper atmosphere. For modeling air drag force, knowledge about the spacecraft relative velocity to the Earth's atmosphere $\boldsymbol{V}$ is needed [1].

$$\boldsymbol{F}^i_{\text{aero}} = \frac{1}{2}\rho\, C_d\, \boldsymbol{S}_i\, \boldsymbol{V}^T\boldsymbol{V} \tag{2.11}$$

Magnetic torque

The torque generated by a magnetic dipole $\boldsymbol{m}$ in a magnetic field $\boldsymbol{B}$ can be computed as

$$\boldsymbol{L}_{\text{mag}} = \boldsymbol{m} \times \boldsymbol{B} \tag{2.12}$$

Magnetic torque can be used as control input when magnetorquers are used for attitude control. For the satellite used in this thesis magnetorquers are used for momentum management of the satellite, which is described in subsection 3.6. Undesirable magnetic dipoles of construction can lead to magnetic disturbance torques affecting the attitude.

Usually $\boldsymbol{L}_{\text{mag}}$, $\boldsymbol{m}$ and $\boldsymbol{B}$ is expressed in body coordinate system. There are several ways to determine the body frame magnetic field [1]. For the satellite in this thesis the Earth's magnetic field of the vector is computed from the model of magnetic field, the International Geomagnetic Reference Field. Having knowledge about the satellite attitude a magnetic field vector in the body frame can be expressed. Additionally, this method needs satellite position, which can be measured using an onboard GNSS receiver.

2.4.2 Internal torques

Some spacecraft can be modeled as a single rigid body, but many spacecraft consist of multiple parts connected by joints having one, two, or three degrees of freedom. The satellite used in this thesis consists of the main body, and two flexible deployable solar panels, which are connected to the main body. In this thesis satellite solar panels have been deployed already. The movement of these solar panels generates torque, which rotates the main body of the spacecraft.

Spacecraft in this thesis has reaction wheels that spin and have some angular momentum. These internal torquers are known as momentum exchange torquers. The physical principle is the exchange of momentum between reaction wheels and the spacecraft body. Rotating the spinning reaction wheels can generate torque, which is an undesirable disturbance [1].

Other sources of internal torques for a general satellite can be a result of spacecraft flexibility, using reaction thrusters or a gas leak.

Reaction wheels

Consider that the spacecraft has n wheels. Each reaction wheel is axially symmetric and spins with an angular velocity ω_i around the spinning axis $\boldsymbol{w}_i$. Each one of the reaction wheels has its moment of inertia corresponding to its spinning axis $J_i^{\|}$. Assume that moments of inertia corresponding to the axes perpendicular to the spinning axis are embedded in the spacecraft's moment of inertia matrix $\boldsymbol{J}_B$. Then the momentum of all reaction wheels is expressed by equation 2.13.

$$\boldsymbol{H}^w = \sum_{i=1}^{n} J_i^{\|} \left(\boldsymbol{w}_i \cdot \boldsymbol{\omega}_I + \boldsymbol{\omega}_i\right) \boldsymbol{w}_i \tag{2.13}$$

Finally, the dynamics equation, which takes into account the momentum of reaction wheels is modified equation 2.3 as follows:

$$\boldsymbol{J}_B \dot{\boldsymbol{\omega}}_I = \boldsymbol{L}_{\text{ext}} - \boldsymbol{L}_b^w - \boldsymbol{\omega}_I \times (\boldsymbol{J}_B \boldsymbol{\omega}_i + \boldsymbol{H}^w) \tag{2.14}$$

The $\boldsymbol{L}_b^w$ is torque applied in the body frame to reaction wheels.

Solar panels

In this thesis, the spacecraft has two deployable solar panels connected to the spacecraft. Both solar panels are aligned to the body frame $\boldsymbol{b}_3$ axis. This connection and flexibility of solar panels can be approximated by a rotational 1 DOF joint. The joint is modeled using spring-damper analogy [8]. This approach is just linear simplification and flexible dynamics, nonlinearities corresponding to rotating bodies are replaced by this simple linear model.

Each solar panel connection to the main body is modeled by a torsional spring with spring constant k_{pi} and has rotational damper b_{pi}. Each solar panel has a moment inertia corresponding to the joint axis J_{pi}. The state variables describing a panel dynamics are the rotational velocity of the solar panel ω_{pi} and the angle displacement of a panel from its equilibrium position θ_{pi}. The state model for each solar panel can be described by the following linear differential equations.

$$J_{pi}\, \dot{\omega}_{pi} = -b_{pi}(\omega_{pi} - \omega_{I3}) - k_{pi}\theta_i \tag{2.15}$$

$$\dot{\theta}_{pi} = \omega_{pi} - \omega_{I3} \tag{2.16}$$

As can be seen from equations 2.15, 2.16 contribution of rotation of satellite in other axes, the joint axis is neglected. Disturbance torque from solar panel affecting satellite dynamics 2.3 is

$$\boldsymbol{L}_{pi} = (b_{pi}(\omega_{pi} - \omega_{I3}) + k_{pi}\theta_i) \begin{pmatrix} 0 \\ 0 \\ 1 \end{pmatrix} \tag{2.17}$$

Augmenting system 2.3 by solar panel dynamics adds two state variables for each solar panel. The dynamics of a satellite with solar panels can be described by following ODEs.

$$\begin{aligned} \boldsymbol{J}_B\,\dot{\boldsymbol{\omega}}_I &= \boldsymbol{L}_{\text{ext}} - \boldsymbol{\omega}_I \times \boldsymbol{h} - \sum_{i=1}^{2} \boldsymbol{L}_{pi} \\ J_{pi}\,\dot{\omega}_{pi} &= -b_{pi}(\omega_{pi} - \omega_{I3}) - k_{pi}\theta_i \\ \dot{\theta}_{pi} &= \omega_{pi} - \omega_{I3} \end{aligned} \tag{2.18}$$

Chapter 3

Controlled satellite

In this chapter, the controlled satellite, its sensors, actuators, and its flight software including the baseline controller will be presented. Additionally, a control oriented model using equations from chapter 2 will be built and validated with high-fidelity 42 Simulator.

3.1 Overview

The controlled satellite is a 6U 3x2 CubeSat satellite, consisting of six cubes 10cm x 10cm x 10cm. The satellite has attached two solar panels connected along the $\boldsymbol{b}_3$ axis. The camera is mounted along $\boldsymbol{b}_1$ axis, as can be seen from the figure 3.1. From all parameters of the satellite, the most important parameters are $\boldsymbol{J}_B$, J_{p1}, and J_{p2}.

$$\boldsymbol{J}_B = \begin{pmatrix} 0.089 & -0.001 & 0.003 \\ -0.001 & 0.103 & -0.015 \\ 0.003 & -0.015 & 0.071 \end{pmatrix} \text{kg m}^2 \tag{3.1}$$

$$J_{p1} = J_{p2} = 0.005\,\text{kg m}^2 \tag{3.2}$$

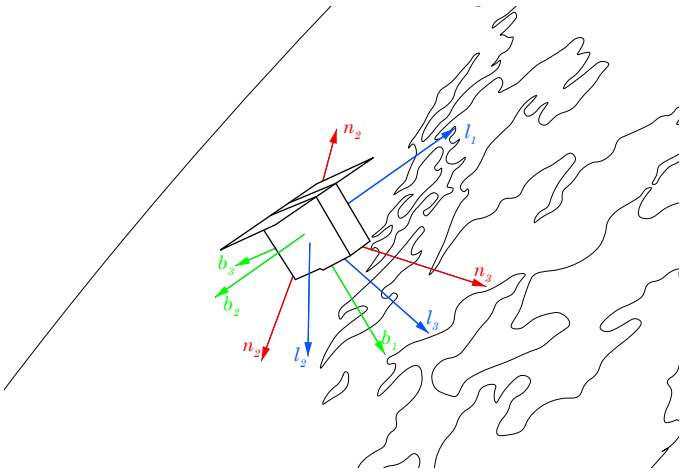

Figure 3.1: Satellite scheme with coordinate systems

3.2 42 Simulator

42 is a comprehensive general-purpose simulation of spacecraft attitude and orbit dynamics developed by an engineer in the Attitude Control Systems Engineering Branch at NASA Goddard Space Flight Center. Its primary purpose is to support the design and validation of attitude control systems, from concept studies through integration and testing. 42 accurately models multi-body spacecraft attitude dynamics (with rigid and/or flexible bodies) and both two-body and three-body orbital flight regimes, modeling environments from low Earth orbit to throughout the solar system. 42 simulates multiple spacecraft simultaneously, facilitating studies of rendezvous, proximity operations, and precision formation flying. It also features visualization of spacecraft attitude [9].

Flight software model is part of 42 Simulator and its structure is described more in detail in the section 3.6. The sensor models support models for star tracker, gyro, and other sensors, with their biases, noises, quantization, etc... Additionally in the simulator are models for actuators used in this thesis. It supports models of magnetorquers and reaction wheels with the saturation of their momentum, torque, etc...

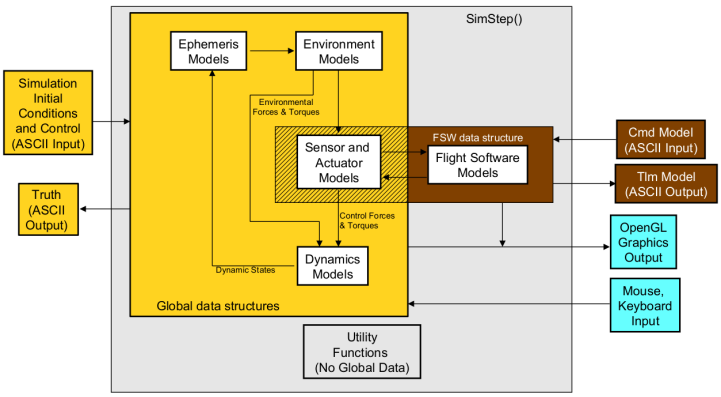

Figure 3.2: Architecture diagram of 42 Simulator

The simulator is open-source and programmed in C, so it is portable across computing platforms. The simulator also supports socket communication so the flight software can run outside the 42 for example in MATLAB. This results in support of model in the loop(MIL) simulations, which were mostly used verifying concepts. For Monte Carlo simulations is flight software model programmed in C for fast evaluation of software in the loop(SIL) simulations. Simulator is in the scope of this thesis used for validation and verification of designed control laws, integrated into the flight software. Developed control-oriented models are validated too.

3.3 Control-oriented model

The control-oriented model will be used for linearization and subsequent design of the controllers. This model uses equations from the chapter 2. In this thesis, two control-oriented models will be used. One model will have flexible appendages modeled. Another one without flexible appendages will be used for state-space methods for controller design. Both models have as input torque in body frame $\boldsymbol{L}_b$ in each axis, which for simplicity and general notation is marked as $\boldsymbol{u}$.

3.3.1 Model without flexible appendages

State vector $\boldsymbol{x}$ consists of six state variables $\boldsymbol{x} = (\omega_{I_x}, \omega_{I_y}, \omega_{I_z}, q_1, q_2, q_3)^T$. The first trio of state variables, marked as $\boldsymbol{x}_\omega$ corresponds to the rotational velocity $\boldsymbol{\omega}_I$. The last three state variables marked $\boldsymbol{x}_q$ correspond to the reduced quaternion $\boldsymbol{q}$.

This model includes pure rotational dynamics described by equation 2.3. Reduced quaternion kinematics for controlability is used, derived in the equation 2.7. Putting these equations together a nonlinear control-oriented model is obtained.

$$\begin{aligned} \dot{\boldsymbol{x}}_\omega &= \boldsymbol{J}_B^{-1}(\,\boldsymbol{u} - \boldsymbol{x}_\omega \times \boldsymbol{h}) \\ \dot{\boldsymbol{x}}_{\boldsymbol{q}} &= \frac{1}{2}\boldsymbol{Q}(\boldsymbol{x}_q)\,\boldsymbol{x}_\omega \end{aligned} \tag{3.3}$$

After linearization at point $\boldsymbol{x}_0 = (0,0,0,0,0,0)^T$ a linear state-space model is obtained

$$\dot{\boldsymbol{x}} = \begin{pmatrix} \boldsymbol{0}_3 & \boldsymbol{0}_3 \\ \frac{1}{2}\boldsymbol{I}_3 & \boldsymbol{0}_3 \end{pmatrix} \begin{pmatrix} \boldsymbol{x}_\omega \\ \boldsymbol{x}_q \end{pmatrix} + \begin{pmatrix} \boldsymbol{J}_B^{-1} \\ \boldsymbol{0}_3 \end{pmatrix} \boldsymbol{u} \tag{3.4}$$

3.3.2 Model with flexible appendages

State vector $\boldsymbol{x} = (\omega_{I_x}, \omega_{I_y}, \omega_{I_z}, q_1, q_2, q_3, \omega_{p1}, \theta_{p1}, \omega_{p2}, \theta_{p2})^T$ consists of ten state variables. The first six state variables have the same meaning as in the previous subsection discussing the model without flexible appendages. The last four state variables describe the dynamics of flexible appendages, see notation from subsection 2.4.2.

This model includes pure rotational dynamics, reduced quaternion kinematics for controlability. Additionally, flexible appendage dynamics from equations is used. When these equations are combined a nonlinear control-oriented model is obtained by rewriting the equation 2.18.

$$
\begin{aligned}
\dot{\boldsymbol{x}}_{\boldsymbol{\omega}} &= \boldsymbol{J}_B^{-1}(\,\boldsymbol{u} - \boldsymbol{x}_{\boldsymbol{\omega}} \times \boldsymbol{h} - \sum_{i=1}^{2}(b_{pi}(\omega_{pi} - x_3) + k_{pi}\theta_i)) \\
\dot{\boldsymbol{x}}_{\boldsymbol{q}} &= \frac{1}{2}\boldsymbol{Q}(\boldsymbol{x}_{\boldsymbol{q}})\,\boldsymbol{x}_{\boldsymbol{\omega}} \\
\dot{x}_7 &= -\frac{b_{p1}(x_7 - x_3) + k_{p1}x_8}{J_{p1}} \\
\dot{x}_8 &= x_7 - x_3 \\
\dot{x}_9 &= -\frac{b_{p2}(x_9 - x_3) + k_{p2}x_{10}}{J_{p2}} \\
\dot{x}_{10} &= x_9 - x_3
\end{aligned}
\tag{3.5}
$$

After linearization at $\boldsymbol{x}_0 = (0,0,0,0,0,0,0,0,0,0)^T$ a linear state-space model can be obtained, see equation 3.6. For clarity of notation a symbol for vector $\tilde{\boldsymbol{J}} = \boldsymbol{J}_{B_{(:,3)}}^{-1}$ is introduced. It is the last column of the satellite's moment of inertia matrix inversion.

$$
\begin{aligned}
\dot{\boldsymbol{x}} &= \boldsymbol{A}\,\boldsymbol{x} + \boldsymbol{B}\,\boldsymbol{u} \\
\boldsymbol{A} &= \begin{pmatrix}
[\mathbf{0}_{3\text{x}2}, -(b_1+b_2)\tilde{\boldsymbol{J}}] & \mathbf{0}_3 & \tilde{\boldsymbol{J}}b_1 & \tilde{\boldsymbol{J}}k_1 & \tilde{\boldsymbol{J}}b_2 & \tilde{\boldsymbol{J}}k_2 \\
\frac{1}{2}\boldsymbol{I}_{3\text{x}2} & \mathbf{0}_3 & \mathbf{0}_{3\text{x}1} & \mathbf{0}_{3\text{x}1} & \mathbf{0}_{3\text{x}1} & \mathbf{0}_{3x1} \\
[\mathbf{0}_{1\text{x}2}, b_1] & \mathbf{0}_{1\text{x}3} & -b_1 J_{p1}^{-1} & -k_1 J_{p1}^{-1} & 0 & 0 \\
[\mathbf{0}_{1\text{x}2}, -1] & \mathbf{0}_{1\text{x}3} & 1 & 0 & 0 & 0 \\
[\mathbf{0}_{1\text{x}2}, b_2] & \mathbf{0}_{1\text{x}3} & 0 & 0 & -b_2 J_{p2}^{-1} & -k_2 J_{p2}^{-1} \\
[\mathbf{0}_{1\text{x}2}, -1] & \mathbf{0}_{1\text{x}3} & 0 & 0 & 1 & 0
\end{pmatrix} \\
\boldsymbol{B} &= \begin{pmatrix} \boldsymbol{J}_B^{-1} \\ \mathbf{0}_{7\text{x}3} \end{pmatrix}
\end{aligned}
\tag{3.6}
$$

From simple analysis of the linearized model with flexible appendages can be seen that using non-diagonal moment of inertia matrix $\boldsymbol{J}_B$ distributes the torque from solar panels to the different axes, along which no flexible appendage is mounted. This torque distribution can be also seen in the figure 3.9.

Analyzing modes of the system symmetric and anti-symmetric modes can be recognized, which are typical for systems with flexibility [10]. By looking at the poles of the transfer function of system 3.6 in figure 3.3, can be seen faster and slower oscillatory modes, specifically:

Mode	**Frequency (rad/s)**
Symmetric	4.78
Anti-symmetric	5.04

Table 3.1: Flexible modes of satellite from equation 3.6

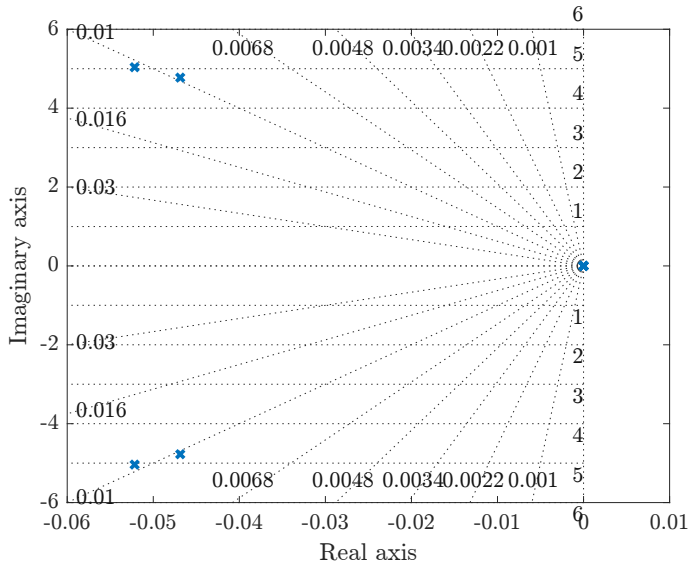

Figure 3.3: Diagram with poles of the linearized system with flexible appendages 3.6

3.4 Actuators

The satellite from this thesis is equipped with two types of actuators, which are regularly used for CubeSats attitude control. In this section reaction wheels and magnetorquers are described briefly.

3.4.1 Reaction wheels

This satellite has four reaction wheels. They can be mounted in different configurations to achieve three-axis control and redundancy. The satellite utilizes a pyramidal configuration, but other reaction wheel configurations can be used [1].

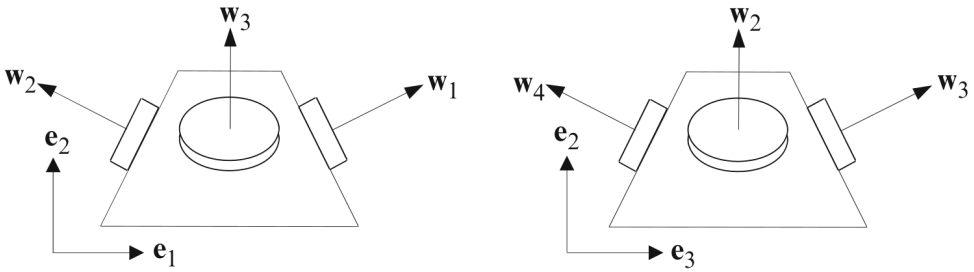

Figure 3.4: Pyramidal configuration of reaction wheels [1]

As was shown in the developed satellite model in the equation 2.14, reaction wheels work on the action and reaction principle. Speeding or slowing down the reaction wheel rotational velocity by applying torque affects the satellite

by the torque in the opposite direction.

Using the knowledge about the mounting axis $\boldsymbol{w}_i$ a relation between torque applied to each wheel L_i^w and torque in body frame $\boldsymbol{L}_b^w$ can be derived using control allocation matrix $\boldsymbol{W} = (\boldsymbol{w}_1, ..., \boldsymbol{w}_n)$ and vector corresponding to the reaction wheels torque $\boldsymbol{L}^w = (L_1^w, ..., L_n^w)^T$. $\boldsymbol{W}^\dagger$ is pseudo-inverse of matrix $\boldsymbol{W}$.

$$\boldsymbol{L}_b^w = \boldsymbol{W}\,\boldsymbol{L}^w \tag{3.7}$$

$$\boldsymbol{L}^w = \boldsymbol{W}^\dagger\,\boldsymbol{L}_b^w \tag{3.8}$$

When using only reaction wheels from a control engineering perspective a problem with reaction wheel saturation arises. A reaction wheel can have limited angular momentum, so its rotational velocity has an upper and lower saturation bound. Additionally in an ideal situation, it is wanted to have the total angular momentum of all wheels as close to zero as possible. In that case, the term for $\boldsymbol{H}^w$ vanishes out from the equation 2.14 and no disturbance torque affects satellite attitude. For mitigation of this effect an actuator commanding subsystem, described in 3.6, or feedforward is used.

Additionally imperfect manufacturing of reaction wheels can cause micro-vibrations. These micro-vibrations can affect the performance of the attitude control subsystem [11]. In the scope of the thesis, micro-vibrations mitigation is out of the scope of attitude control and is solved by mechanical construction.

3.4.2 Magnetorquers

Magnetorquers are planar coils. When electricity passes through the coil a magnetic dipole is created. The generated magnetic dipole is dependent on several variables such as the electric current passing through the coil, the number of turns, and the area enclosed by the coil. The resulting control torque is determined by the same equation 2.12 as for magnetic disturbance torque [7].

The benefit of using magnetorquers is, that they do not have any moving parts, they are more reliable. The disadvantage of using magnetorquers is that the generated torque depends on the position of the satellite in the Earth's magnetic field. Additionally, the satellite can not be controlled in all three axes because the generated magnetic control torque is perpendicular to the vector of the Earth's magnetic field.

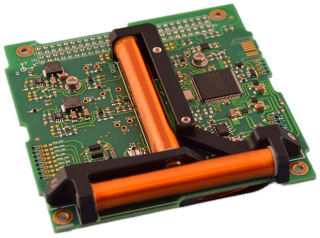

Figure 3.5: Magnetorquer module [2]

3.5 Sensors

Satellite uses multiple sensors for the correct functionality of the attitude control subsystem. In this section main sensors used for fine pointing scenario are described.

Star Tracker

Star tracker sensor is a digital camera modified to capture stars. This sensor provides information about the spacecraft's attitude and rotational velocity concerning a celestial reference frame with an accuracy of a few arcseconds. The sensor has two modes: tracking and initial attitude acquisition. In the initial attitude acquisition mode sensor compares measurements with the star catalogue stored onboard the star tracker. In the tracking mode sensor tracks several stars from the catalogue [1].

From the sensor description, it is clear, that this sensor does not like big rotational speeds. Therefore this sensor is used in the fine pointing scenario and during slow maneuvers. Additionally, a star tracker works if and only if stars are in its field of view. So this sensor is not available every time and its position within satellite construction has to be optimized to achieve mission specification and best performance.

Figure 3.6: Star Tracker [3]

Model of the sensor shown in the figure 3.6 is used in 42 Simulator. From all types of data and measures from the datasheet, I selected measurement noise measure, which has 3σ in axes $(9, 9, 51)$ arcsec. This star tracker is more noisy in the z axis, which causes a noisier control error in the z axis. This is shown when designed controllers will be evaluated in part III.

Gyroscope

The sensor of rotational velocity used in this satellite is a MEMS gyroscope with all its advantages and drawbacks. The benefits of using MEMS gyro is its cost and size. A disadvantage is gyroscope bias, which has to be removed, but this is not in the scope of this thesis. For the satellite gyroscope measurement of the rotational velocity of the satellite is more accurate than star tracker rotational velocity measurement. Therefore, a gyroscope is used as a source of rotational velocity.

GNSS

The onboard GNSS receiver is used to measure satellite position. The measured position is important to compute Earth's magnetic field vector for using magnetorquers. Additionally, knowledge about the satellite position is crucial for coordinate systems transformations and satellite guidance algorithms, for example, an object tracking scenario.

Advanced acquisition of GNSS signal based on measuring the magnitude of the carrier wavelength directly, can be used for satellite attitude determination described in [1]. This method is not used for the satellite in this thesis.

3.6 Flight software

Model of flight software is implemented in C. Flight software consists of multiple components used for fine pointing or object tracking scenario.

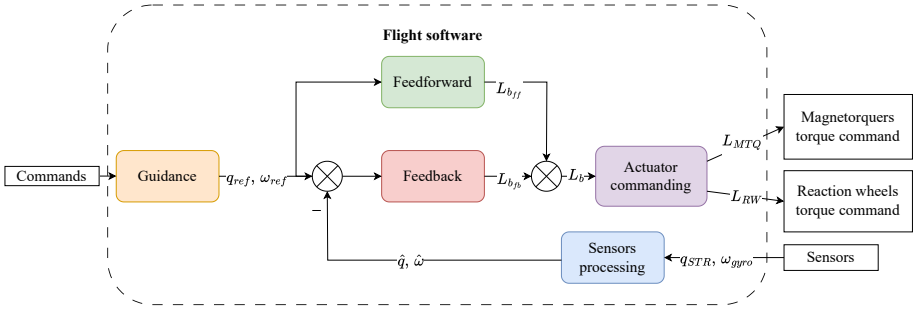

Figure 3.7: Flight software architecture diagram

Sensor processing

In this module sensor measurements from the star tracker and gyro are transformed from the sensor frame to the body frame. Additionally, calibration transformations are applied to measured data. In this thesis, no Kalman filter is used to estimate the state vector of the satellite.

Additionally the reaction wheel speed is measured and the GNSS position too, which is not shown for simplicity of the diagram.

Guidance

Guidance algorithms have commands for the satellite at the input. The guidance algorithm outputs reference signals for quaternion and rotational speed in the inertial frame. Commands for fine pointing are pointing to the specific attitude in the inertial or orbital frame. In the case of pointing in the orbital frame, attitude reference in the inertial frame is time variant, so a constant reference is not tracked in this case.

Additionally guidance algorithms calculate reference to attitude and rotational velocity for object tracking scenario, so spacecraft points all the time to the same place for example during communication with a ground station, when a directional antenna is used.

To sum up, the guidance subsystem supports these commands:

- Tracking attitude commands in LVLH frame
- Tracking attitude commands in the inertial frame
- Object tracking, object position is given in ECEF frame.

Feedforward

Feedforward is implemented to improve reference tracking. After the second derivation of quaternion reference signals, feedforward computes control torque to achieve reference tracking. Using the equation 2.14 torque $\boldsymbol{L}_b^w$ for specific $\boldsymbol{\omega}_{ref}$ or $\dot{\boldsymbol{\omega}}_{ref}$ can be found. Additionally, feedforward can be used to mitigate the effect of angular momentum of reaction wheels, by using the information about reaction wheels speed.

Feedback

The feedback controller outputs torque command in the body frame and computes it from the control error of quaternion $\boldsymbol{\delta q}$ and rotational velocity $\boldsymbol{\delta\omega}$. Quaternion control error which shall be driven to unit quaternion (i.e. reference $\boldsymbol{q}_{ref}$ and body quaternions $\hat{\boldsymbol{q}}$ are matching) and corresponding angular rate control error which shall be driven to zero (body angular rate $\hat{\boldsymbol{\omega}}$ is equal to reference angular rate $\boldsymbol{\omega}_{ref}$) are computed as

$$\boldsymbol{\delta q} = \hat{\boldsymbol{q}} \otimes \boldsymbol{q}_{ref}^{-1} \tag{3.9}$$

$$\boldsymbol{\delta\omega} = \hat{\boldsymbol{\omega}} - \boldsymbol{\omega}_{ref} \tag{3.10}$$

Using reduced quaternion notation a relation for quaternion control error from 3.9 can be rewritten into a reduced quaternion control error, shown in the equation 3.11[7].

$$\boldsymbol{\delta q} = \mathrm{sgn}(\delta q_0)\boldsymbol{\delta q}_{1:3} \tag{3.11}$$

For small angles, in the neighborhood of linearization point, an equation 3.9 can be simplified as $\boldsymbol{\delta q} = \hat{\boldsymbol{q}} - \boldsymbol{q}_{ref}$.

The baseline feedback control law used for the satellite is designed for each axis separately using the pole placement method. Poles were placed using state feedback. For SISO design state variables are quaternion and rotational velocity. These three controllers can be rewritten into the matrix form using constant matrix $\boldsymbol{K}_{\text{SISO}} = (\boldsymbol{K}_\omega, \boldsymbol{K}_q)$, which consists from two diagonal matrices, one for rotational velocity error and the second one for reduced quaternion error. The feedback control law is given by equation .

$$\boldsymbol{L}^w_{b_{fb}} = -\boldsymbol{K}_{\mathbf{SISO}} \left(\boldsymbol{\delta\omega}, \boldsymbol{\delta q}\right)^T \tag{3.12}$$

This controller will be validated in high-fidelity simulation and compared to the designs developed in this thesis in part III.

Actuator commanding

The actuator commanding subsystem consists of functions, that support the allocation of requested control torque. It is the output of the feedback controller and feedforward term.

In the equation 3.8 is shown, how torque for each reaction wheel is computed using the pseudo-inverse of control allocation matrix $\boldsymbol{W}^\dagger$. Additionally to this reaction wheel torque is added null space torque, which balances reaction wheel speeds in the direction of the null-space vector of the control allocation matrix. This null-space control technique is described in depth in [12].

Magnetorquers are commanded by momentum management algorithm in a way, to minimize total momentum of all reaction wheels by creating additional magnetic "disturbance" torque in such direction, so the reaction wheel speeds can balance them and won't saturate. More about this algorithm can be found in [13].

3.7 Model validation

In this section are compared responses of developed nonlinear control-oriented models with responses from 42 Simulator.

3.7.1 Satellite dynamics and kinematics in inertial frame

For this comparison are environment torques disabled and the connection of satellite solar panels is considered as rigid in the simulator. Nonlinear state-space model 3.3 is used. During validation satellite performs a maneuver of changing its attitude with baseline feedback controller described in the 3.6. In the simulation, an ideal torque in body frame $\boldsymbol{L}_b$ is applied, and no actuator commanding is used. This is to not introduce any errors. During

the validation experiment satellite was commanded to tilt by 30° on each axis and then 30° in all axes.

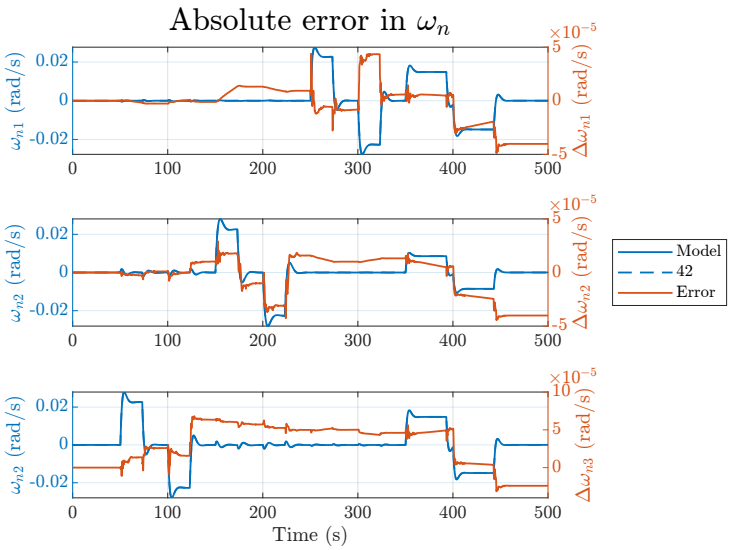

Figure 3.8: Comparison of error between 42 response and developed model 3.3

From figure 3.8 can be seen that the model fits well the 42 response. The absolute error is in order three times smaller than rotational velocity and the differences are caused by numerics.

3.7.2 Solar panels model

For this comparison environment torques are disabled. The connection of satellite solar panels with the satellite main body is not rigid. Dynamics of spacecraft from equation 3.5 is used.

During validation, the satellite performs a maneuver of changing its attitude with the baseline feedback controller. In the simulation an ideal torque in body frame $\boldsymbol{L}_b$ is applied as control input.

In the figure 3.9 can be seen a detail of simulated responses. It is a maneuver of changing attitude by 30° around the $\boldsymbol{b}_3$ axis, the axis of mounting solar panels. The frequency and damping are captured. There is a small error in the amplitude of the developed model. Additionally the are induced oscillations along axes $\boldsymbol{b}_1$, $\boldsymbol{b}_2$. These oscillations are induced by cross-coupling because the moment of inertia matrix $\boldsymbol{J}_B$ is not diagonal. These oscillations are not captured correctly because of the simplicity of the model, but their amplitude is small and can be neglected.

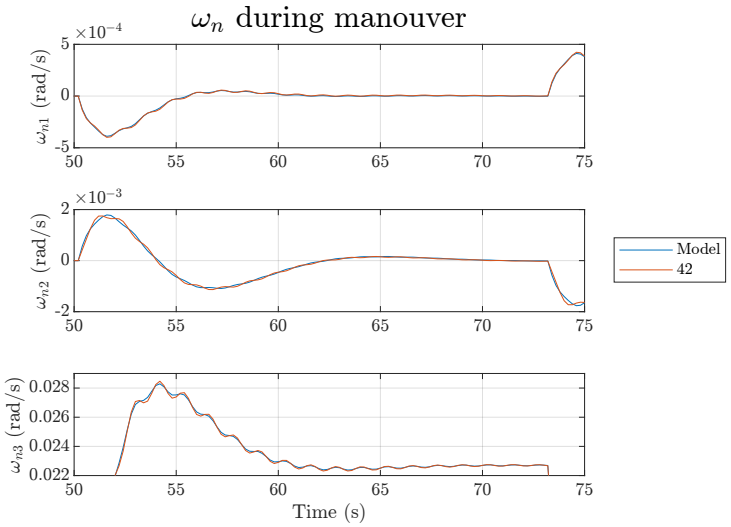

Figure 3.9: Detailed view of responses from 42 and developed model 3.5 during maneuver

3.7.3 Environment disturbances identification

In this subsection, environment disturbances are identified using simulation data from 42 simulator. These disturbance models are used for satellite dynamics derived in the inertial frame.

For environmental torques identification and demonstration purposes satellite was commanded to hold different attitude angles in the orbital frame. The commanded angles are in range of $\pm 45°$ in each axis from nadir direction $\boldsymbol{q}_{\text{nadir}} = (1, 0, -1, 0)^T$.

Gravity gradient

If the satellite dynamics is developed in the inertial frame, it is not easy to find an analytical formula for gravity gradient, because this disturbance torque is dependent on the position of the satellite, and then the system would be time variant, when no translation dynamics is modeled. There is an exception in case, the satellite holds attitude in the orbital frame.

As can be seen from the equation 2.9 when the attitude of the satellite in the orbital frame does not change, gravity gradient torque is constant. So gravity gradient torque can be modeled as constant torque in each axis. The amplitude of the torque acting on the satellite depends on the attitude in the orbital frame and can be seen in the figure 3.11. The constant dependence of disturbance torque on time can be seen.

The maximum mean gravity gradient torque amplitude 68.3 nNm affecting the spacecraft was measured in the following attitude perturbations from nadir direction $(-45°, -45°, -45°)^T$, $(0°, -45°, -45°)^T$, $(45°, -45°, -45°)^T$. For the nadir direction gravity gradient torque affecting the spacecraft is 10.6 nNm.

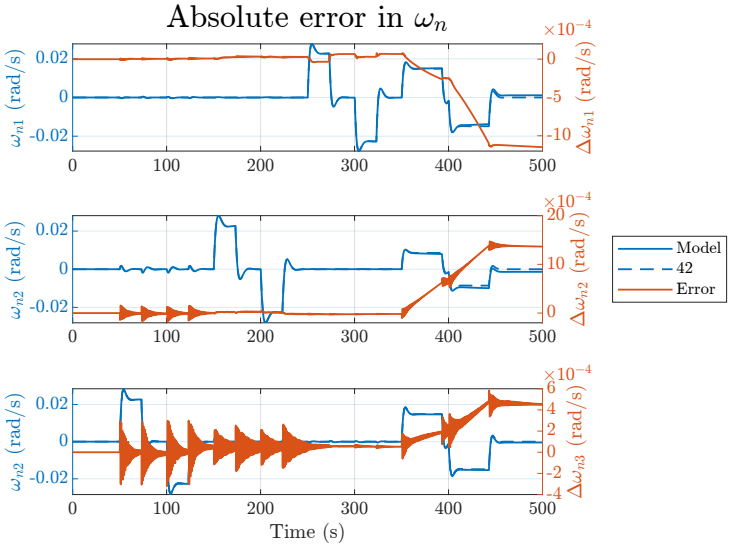

Figure 3.10: Comparison of error between 42 response and developed model with solar panels dynamics 3.5

Aerodynamic torque

Taking into account the complexity and uncertainty of modeling the aerodynamic torque from equation 2.11 the aerodynamic torque can be modeled by frequency characteristic of the disturbance torque. Assuming fixed attitude in an orbital frame while orbiting the Earth the dominant terms in the Fourier analysis of the aerodynamic disturbance torque signal are the DC and the twice orbit rate terms as can be seen from the figure 3.12. The DC part is a contribution of the fixed attitude in the orbital frame, so $\boldsymbol{S}_i$ does not change while orbiting. The second harmonic of orbit rate is because the velocity $\boldsymbol{V}$ changes twice. Once when a satellite travels from north to south and vice versa. In Fourier analysis can be observed disturbance torque at the orbital rate frequency because the atmospheric density varies each orbit [14].

Shape of the aerodynamic disturbance torque magnitude in the time domain can be seen in figure 3.13. The experiment is the same as in the previous part of the subsection 3.7.3. The maximum mean value of disturbance torque during one orbit is 1.16 μNm for attitude perturbation $(0°, -45°, 0°)^T$ degrees. For perturbations $(45°, -45°, -45°)^T$ $(-45°, -45°, 45°)^T$ the mean torque is 1.13 μNm.

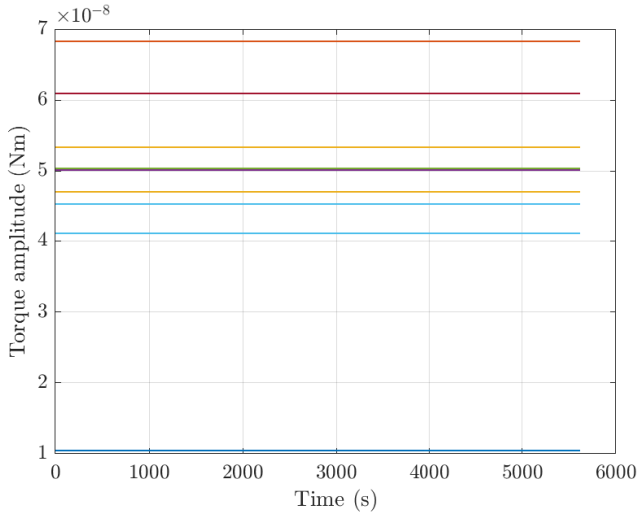

Figure 3.11: The amplitude of gravity gradient torque for holding different attitude commands

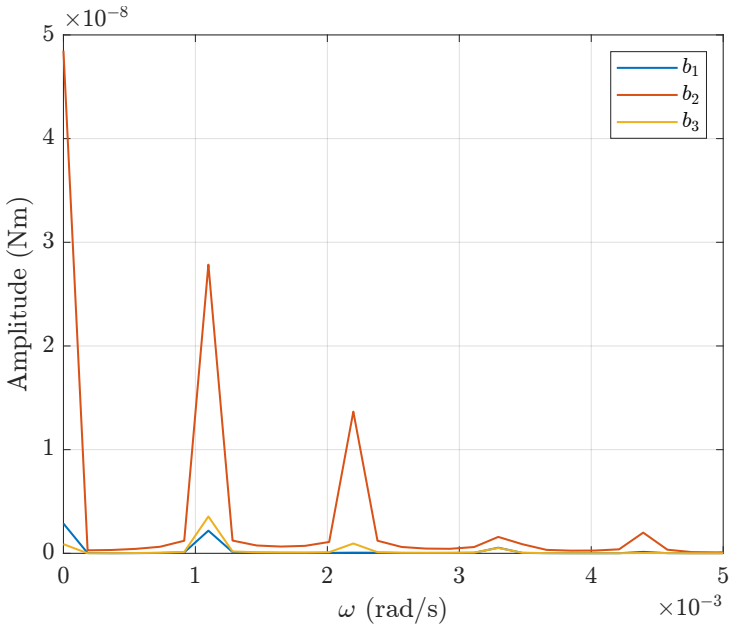

Figure 3.12: Fourier analysis of aerodynamic disturbance torque acting on spacecraft with respect to body axes in nadir attitude

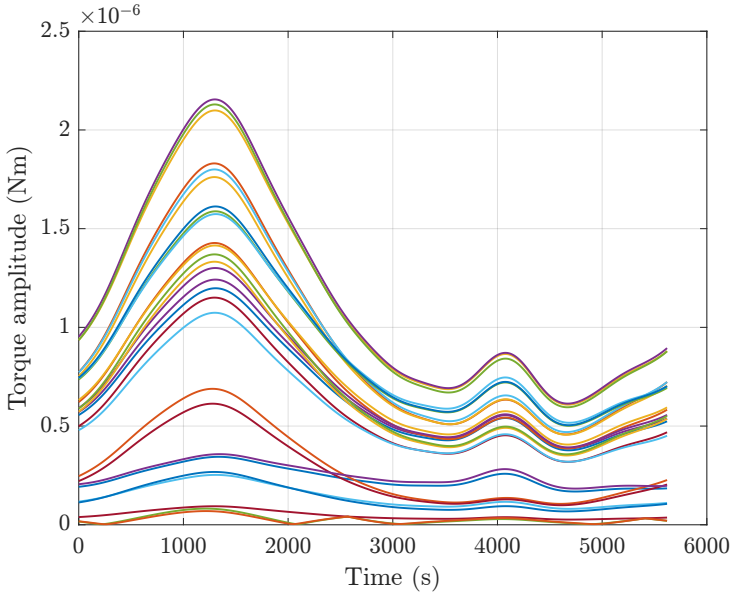

Figure 3.13: Amplitude of aerodynamic torque for different attitude commands

Magnetic torque

As can be seen in the equation 2.12 relation for magnetic torque is complex and time variant and it is difficult to include this torque into the control-oriented model. As can be seen from the following analysis, magnetic torque is the major disturbance torque acting on the spacecraft in nadir attitude. Its analysis in the frequency domain is important for disturbance rejection.

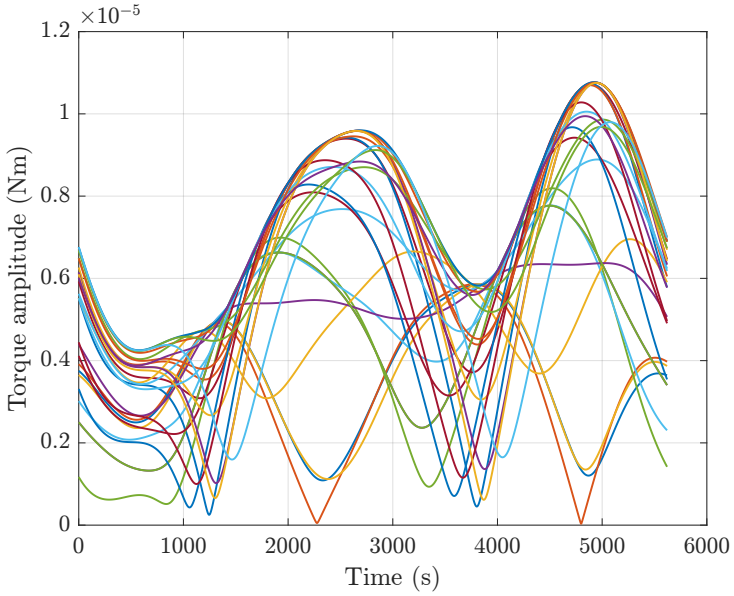

Figure 3.14: Amplitude of magnetic torque for different attitude commands

The maximum mean value of disturbance torque during one orbit is 7.42

for attitude perturbation $(-45°, -90°, 45°)^T$ degrees. For the nadir direction, magnetic torque affecting the spacecraft is $5.76\,\mu$Nm.

3.7.4 Environment disturbances overview

From the results shown in the previous subsection 3.7.3 there is a brief overview in this subsection.

Disturbance type	Maximum mean torque at attitude perturbation	Mean torque at nadir
Gravity gradient	68.3 nNm $(-45°, -45°, -45°)^T$ $(0°, -45°, -45°)^T$ $(45°, -45°, -45°)^T$	10.6 nNm
Aerodynamic	$1.16\,\mu$Nm $(0°, -45°, 0°)^T$	49.2 nNm
Magnetic	$7.42\,\mu$Nm $(-45°, -90°, 45°)^T$	$5.76\,\mu$Nm

Table 3.2: Environment disturbance torques overview

As can be seen in the table 3.2 the major disturbance for the spacecraft pointing nadir direction is magnetic torque disturbance which is bigger by two orders than the other two torques. The weakest disturbance is gravity gradient torque, which is additionally constant for constant attitude in the orbital frame. Aerodynamic torque varies in magnitude significantly by two orders and its effect on the spacecraft's attitude can't be neglected in some certain attitudes.

After summing all environmental torques, for spacecraft pointing nadir direction, which are not included in the control-oriented model, I get an overall disturbance torque signal affecting the spacecraft attitude. As will be shown in subsection 5.2, Fourier analysis of this signal, depicted in figure 3.15, is important for the performance of the designed controller. The frequencies at which the overall disturbance is mostly visible are the first, second, and third harmonic of an orbit rate ω_O. A similar approach for obtaining the disturbance model from a nonlinear simulator in the frequency domain was used in the development of ADCS subsystem for MIT ExoplanetSat mission [15]

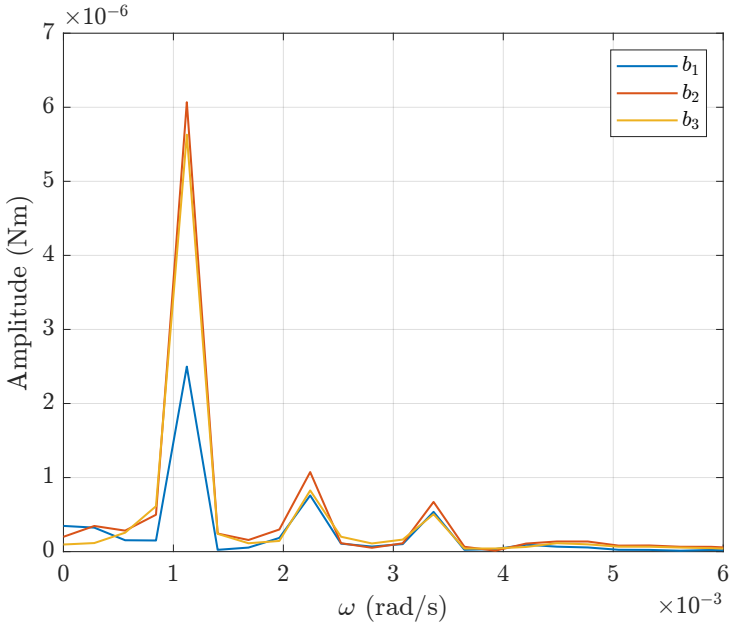

Figure 3.15: Fourier analysis of sum of all disturbance torques acting on spacecraft with respect to body axes in nadir attitude

Part II

Attitude controllers design

Chapter 4

Attitude controller requirements

This chapter introduces the requirements for the feedback controller. The feedback controller is required to reject disturbance torques as analyzed in section 3.7.4. Furthermore, the controller should meet the mission pointing requirements for the attitude control subsystem, such as absolute performance error and relative performance error. Since the parameters of the satellite are not measured accurately and details about the solar panel joints are uncertain, the controller should be designed to be robust to parametric uncertainties. Additionally, the controller should respect the saturation constraints of the actuators. Controller performance and stability will be validated in 42 Simulator with flight software model in part III

4.1 Closed loop controlled system

In a general closed-loop controlled system, the outputs of the plant are measured through a set of sensors, from which the controller computes the physical feedback commands to be applied to the plant by a set of actuators [16].

There are multiple ways how to notate a feedback loop. For the controller design purposes of this thesis, two configurations are used. A one degree-of-freedom control configuration with negative feedback. The second one is a general control configuration.

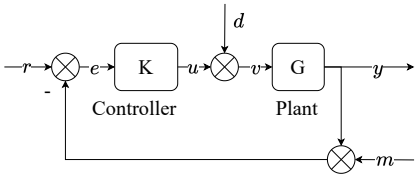

(a) : One degree-of-freedom control configuration

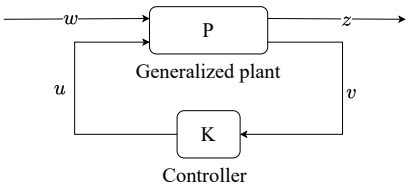

(b) : General control configuration

Figure 4.1: Control configurations

In the classical one-degree-of freedom control configuration can be distinguished several signals and systems:

G	plant model
K	controller
r	reference inputs
d	disturbance signals
u	control signal
v	plant input/total action
m	measurement noise
y	plant output

In the general control configuration can be distinguished several signals and systems:

P	generalized plant model
w	exogenous inputs
z	exogenous outputs
v	controller inputs for general configuration
u	control signals

The controller can be designed to achieve multiple objectives, including stability, tracking, regulation, and sensitivity [17]. In this thesis, the main objectives for the fine pointing controller are regulation and stability. Transfer functions can be derived from a general feedback loop, allowing analysis of the behavior of the closed-loop system. In this context, $L_i = KG$ and $L_o = GK$ are open-loop transfer functions.

- **Output sensitivity** S_o is a closed loop transfer function between the control reference r and the control error e.

$$S_o = \frac{1}{1 + L_o} \tag{4.1}$$

- **Input sensitivity** S_i is a closed loop transfer function between the disturbance d and total action v.

$$S_i = \frac{1}{1 + L_i} \tag{4.2}$$

- **Output complementary sensitivity** T_o is a closed loop transfer function between the control reference r and the system output y.

$$T_o = \frac{L_o}{1 + L_o} \tag{4.3}$$

- **Input complementary sensitivity** T_i is a closed loop transfer function between the disturbance d and controller output u.

$$T_i = \frac{L_i}{1 + L_i} \tag{4.4}$$

4.2 Stability requirements

Stability requirements for the attitude control system are defined by the standard ECSS-E-HB-60-10A document. According to this document: " stability is the intrinsic property defined as the ability of a system to remain indefinitely in a bounded domain around an equilibrium position or around an equilibrium trajectory when submitted to small external disturbances"[16].

Another formulation can be used, so a continuous LTI system is stable if and only if all of the eigenvalues of its state matrix have strictly negative parts. This definition ensures not only that elements of the output vector are bounded, but also that all of the components of the state vector are bounded.

4.2.1 Margins for SISO LTI systems

According to the ECSS-E-HB-60-10A document SISO LTI stability can be quantified using gain and phase margin and their required values are shown in the table 4.1. Additionally, a metric can be used modulus margin which is defined as the minimum distance from the critical point -1 to the open-loop transfer function L. Another recommended measure is delay margin, which is the maximum value of a pure delay in the loop such that the closed-loop system remains stable.

A disk margin can be also used to quantify stability. This stability measure accounts for simultaneous gain and phase perturbations in a feedback system [18]. It is a very conservative measure that gives a bound on maximal complex perturbation under which the system is stable.

Measure	Value
Gain margin	>6 dB
Phase margin	$> 30°$

Table 4.1: SISO stability margins requirements according to the ECSS-E-HB-60-10A

4.2.2 Margins for MIMO LTI systems

Stability indicators dealing with MIMO systems are based on the sensitivity and complementary sensitivity functions defined in the section 4.1. For these systems margins are characterized by the maximal singular value of the transfer function matrix over the frequency domain, H_∞ norm of the transfer function. Before establishing any MIMO stability margins, the closed-loop system has to be stable. Additionally, required margins can be evaluated by the requirements shown in the table 4.2.

When analyzing MIMO systems disk margin can be used too. In addition to the SISO case, disk margin can be used to find the maximal complex

Measure	Value
$\|T_o\|_\infty$	<6 dB
$\|S_o\|_\infty$	<6 dB
$\|T_i\|_\infty$	<6 dB
$\|S_i\|_\infty$	<6 dB

Table 4.2: MIMO stability requirements according to the ECSS-E-HB-60-10A

perturbation at input/output or input-output within all loops [18]. In this thesis under term disk margin is understood as input-output disk margin.

4.2.3 Stability and stability margins verification

An ECSS-E-HB-60-10A document gives a guide to verify stability and stability margins. The process of verification can be split into the following steps:

1. Linearization of the system in the neighborhood of its operational conditions.
2. Design a controller with respect to the linearized system.
3. Verifying system properties(stability, margins,...) using linear analysis techniques, taking into account parametric uncertainties of the system.
4. Validation by performing simulations with the complete system, nonlinear dynamics, actuator nonlinearities, etc. In the scope of this thesis, a 42 simulator is used.

ECSS-E-HB-60-10A document recommends perturbing the following parameters:

- rigid inertia matrix of the satellite
- solar panels coefficients

Depending on the complexity of the system it can be challenging to search for the worst case parameters permutation, so the Monte Carlo approach can be used [16].

In this thesis dynamic model of the satellite is parameterized with 9 parameters defining the moment of inertia matrix and 6 parameters describing flexible solar panels. It is a good practise to perturb each parameter in the range of 50% of the nominal value.

4.3 Performance requirements

4.3.1 ECSS Error indices

ECSS standards recognize performance error e_p and knowledge error, which is out of the scope of this thesis. Performance error definition depends on the application. For attitude control, a performance error is defined in the equation 4.5.

$$e_p = \boldsymbol{q}_{\text{true}} \otimes \boldsymbol{q}_{\text{ref}}^{-1} \tag{4.5}$$

Having defined performance error, ECSS standards recognize multiple error indices such as absolute performance, mean performance, relative performance error, etc.

Absolute performance error - APE

The APE at time t is defined as the value of the performance error t

$$APE(t) = e_p(t) \tag{4.6}$$

Mean performance error - MPE

MPE is defined as a mean value of performance error over a specific time interval.

$$MPE(t, \Delta t) = \frac{1}{\Delta t} \int_{\Delta t} e_p(t)\, dt \tag{4.7}$$

Relative performance error - RPE

RPE is defined as the difference between the instantaneous performance error at a given time, and its mean value over over a time interval containing that time.

$$RPE(t, \Delta t) = e_p(t) - \frac{1}{\Delta t} \int_{\Delta t} e_p(\tau) d\tau,\ \tau \in \Delta t \tag{4.8}$$

RPE is always defined over some period of time. In this thesis is fixed $\Delta t = 1s$.

4.3.2 Mission requirements

Performance requirements are defined by mission goals. For the scenario of this thesis controller is utilized for Earth object tracking, to track the ground station while communicating with the ground station, and fine pointing scenario to capture with a camera the Earth or some part of the sky. Performance requirements for this mission are shown in the table 4.3.

Measure	Scenario	Value
APE (arcsec)	Fine pointing	346
	Object tracking	1800
RPE (arcsec)	Fine pointing	36
	Object tracking	180

Table 4.3: Mission performance requirements

Chapter 5

State-Space design

5.1 State feedback

One of the methods used for controller design is state feedback. State feedback will be designed using the MIMO system description, so control law will take into account non-diagonal elements of satellite moment of inertia matrix $\boldsymbol{J}_B$.

One of the conditions for state feedback is to have information about all states of the system. This can be achieved directly when system states can be measured. In this scenario, both attitude quaternion and angular velocity are measured. Another option is to use an observer to estimate system states. This approach is not used in this thesis, because the frequency of the flexible modes will be shifted by parametric uncertainties and an observer will not behave as expected. Additionally, it gives complexity to the design.

Condition on measuring system states gives a first restriction put on state feedback controller. Because of not measuring states of the solar panels, a simplified linear model not including flexible appendages given by equation 3.4 will be used. So controller will be designed without having knowledge about the flexible dynamics.

An advantage of using a state feedback controller is that it does not increase the order of the system and computing state feedback control law is simple as matrix multiplication.

Designing a state feedback control law for a MIMO system is not easy, especially if a system has three inputs and six outputs. It is not easy to find the location of closed-loop poles in such a way, that closed-loop system will fulfill requirements on performance and stability. To tackle this problem an optimization problem 5.1 has to be solved. This will be assured by minimizing the quadratic cost function by manipulating input $u(t)$. In this thesis generally known as LQR optimal control problem with a free final state and infinite time horizon is selected to find the optimal input signal.

$$\begin{aligned} &\min_{u(t)} \int_0^\infty \boldsymbol{x}(t)^T \boldsymbol{Q}\boldsymbol{x}(t) + \boldsymbol{u}(t)^T \boldsymbol{R}\boldsymbol{u}(t) dt \\ &\text{s.t. } \dot{\boldsymbol{x}} = \boldsymbol{A}\boldsymbol{x} + \boldsymbol{B}\boldsymbol{u} \end{aligned} \tag{5.1}$$

The solution of this problem is a control law in the form of linear time-invariant state feedback $\boldsymbol{u}(t) = -\boldsymbol{K}\boldsymbol{x}(t)$, where $\boldsymbol{K} = \boldsymbol{R}^{-1}\boldsymbol{B}^T\boldsymbol{S}$ and $\boldsymbol{S}$ is a solution of algebraic Riccati equation(ARE)[19].

Solution of Ricatti equation has two conditions. The first one is that a pair of matrices $\boldsymbol{A}$, $\boldsymbol{B}$ must be stabilizable. And pair $\boldsymbol{A}$ and $\sqrt{\boldsymbol{Q}}$ detectable.

To sum up, using LQR to obtain a state feedback matrix by tuning matrices $\boldsymbol{Q}$ and $\boldsymbol{R}$ will simplify the design of the controller instead of placing poles to locations selected by designer. Unfortunately, these matrices do not affect APE and RPE directly, so they have to be tuned to satisfy controller absolute and relative performance errors. An advantage of this method is that LQR guarantees stability margins. Usually $GM > 6\,dB$ and $PM > 60°$.

5.2 Disturbance rejection

For small angles, which arcseconds are, APE is just a control error of reduced quaternion $\boldsymbol{e}_q = \boldsymbol{q}_{\text{ref}} - \boldsymbol{q}_m$, where $\boldsymbol{q}_m$ is measured quaternion. A transfer function $\boldsymbol{D}(j\omega)$ from input disturbance signal d, see notation in a configuration in figure 4.1a, to quaternion control error using input sensitivity function can be derived. Matrix $\boldsymbol{C}$ selects from state vector $\boldsymbol{x}$ only quaternion elements.

$$\boldsymbol{D} = -\boldsymbol{C}\boldsymbol{G}\boldsymbol{S}_i \tag{5.2}$$

In the subsection 3.7.4 a disturbance signal was analyzed in a frequency domain. From this analysis, it is known, that for disturbance rejection is important to attenuate disturbance at the frequencies of first, second, and third harmonic of orbit rate ω_O.

A simple worst-case estimate of an effect of disturbance on APE can be computed using the amplitude of disturbance and maximal singular value of transfer function $\boldsymbol{D}$ at mentioned frequencies.

$$\text{APE}_{\text{est}} = k\sum_{i=1}^{3} d(\omega_{Oi})\overline{\sigma}(\boldsymbol{D}(\omega_{Oi})) \tag{5.3}$$

The relation is scaled by factor k, that is a simple linear transformation gain from quaternion to arcseconds, in which is APE usually given. For small angles, a relation that $\alpha = 2q$ is valid, where α is in radians. Transforming radians to arcseconds is just a transformation from radians to degrees and then multiplying it by 3600.

$$k = 2\frac{180}{\pi}3600 = \frac{1296000}{\pi} \tag{5.4}$$

5.3 Reference tracking

A disadvantage of a state feedback controller is that in general, it is not good for tracking, but for stabilization. To achieve good tracking an integral

control is used. Another approach is to use an introducing reference input with the state feedback concept presented in [17].

This approach will result in zero steady-state error to a step command, but the result is not robust. In case of any change of system parameter, this would result in a non-zero steady state error.

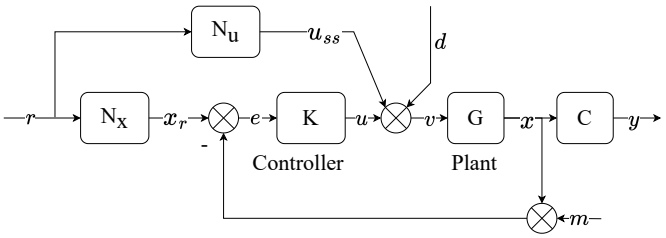

Figure 5.1: Diagram for introducing reference input with state feedback

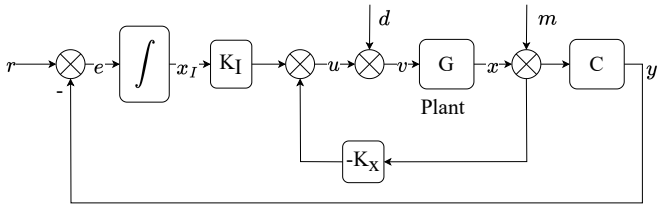

Figure 5.2: Diagram for integral control

To obtain robust tracking, an integral control will be used. Additionally adding an integral term improves disturbance rejection at lower frequencies than the SISO designed baseline controller. For observing the Earth and communicating with the ground station an attitude is important. So attitude error will be integrated. To design a state feedback control law with included integral action, a state-space representation 3.4 has to be augmented by integrated control error. This can be interpreted as adding new state variables $\boldsymbol{x}_I$, so state vector of augmented system is $\boldsymbol{x}_{\text{aug}} = (\boldsymbol{x}, \boldsymbol{x}_I)^T$.

Augmented state-space representation 5.5 will be used in LQR optimal control problem, to design a state feedback matrix $\boldsymbol{K} = (\boldsymbol{K}_x, \boldsymbol{K}_I)$.

$$\dot{\boldsymbol{x}}_{\text{aug}} = \begin{pmatrix} \boldsymbol{A} & \boldsymbol{0}_{6\text{x}3} \\ \boldsymbol{C} & \boldsymbol{0}_{3\text{x}3} \end{pmatrix} \begin{pmatrix} \boldsymbol{x} \\ \boldsymbol{x}_I \end{pmatrix} + \begin{pmatrix} \boldsymbol{B} & \boldsymbol{0}_{6\text{x}3} \\ \boldsymbol{0}_{3\text{x}3} & -\boldsymbol{I}_3 \end{pmatrix} \begin{pmatrix} \boldsymbol{u} \\ \boldsymbol{r} \end{pmatrix} \tag{5.5}$$

5.4 Controller design

The controller in fine pointing mode for fine pointing and object tracking using state feedback was designed using integral control. Poles were placed

by solving the LQR optimal control problem. I selected diagonal matrices. The matrices selected by tuning are:

$$\begin{aligned} \boldsymbol{Q} &= 100\,\mathrm{diag}(0.001,\ 0.0001,\ 0.0001,\ 70,\ 70,\ 70,\ 0,\ 0.001,\ 0.001) \\ \boldsymbol{R} &= 10^7\,\mathrm{diag}(1,\ 5\,10) \end{aligned} \tag{5.6}$$

As can be seen, rotational velocity and quaternion error integral are not penalized the same for each axis. This different weighting helped to decrease singular values of closed-loop transfer functions, but a performance error still meets the performance requirements. x axis is more penalized in terms of rotational velocity and less integral of quaternion error because it is a camera axis and it is not important if the image is rotated, but the image can't be blurred.

A quaternion and rotational velocity control error is fed directly into the controller, as can be seen in the figure 5.3. The reason for this is the fixed structure of the control pipeline in the developed flight software. The controller has on input just a control error. Additionally, this increases bandwidth, so controller agility is better, but more measurement noise will be put into the system.

In this case controller is not just matrix gain, but it has integrator dynamics. To rewrite it compactly controller $\boldsymbol{K}$ can be expressed as:

$$\boldsymbol{K}(s) = \begin{pmatrix} \boldsymbol{K}_{x_\omega} & \boldsymbol{K}_{x_q} + \frac{1}{s}\boldsymbol{K}_I \end{pmatrix} \tag{5.7}$$

Looking at the structure of $\boldsymbol{K}$ and taking into account the knowledge from linearized quaternion kinematics that $\dot{q} = 0.5\omega$, it can be interpreted that controller $\boldsymbol{K}$ is a matrix of virtual PID controllers.

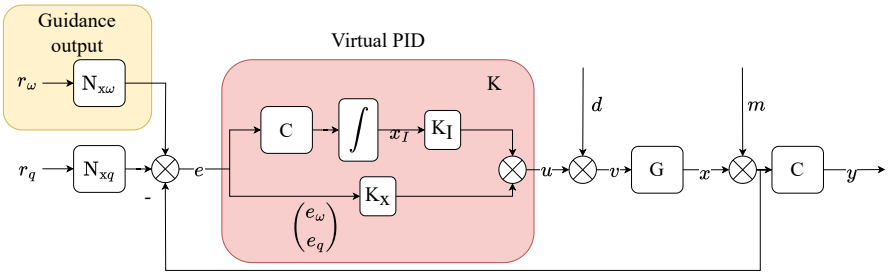

Figure 5.3: Scheme of control loop using LQR with integral control designed controller

There are several matrices in this control diagram, to ensure that specific reference signal, will correctly generate reference state vector and have correct dimensions. This concept was introduced in the previous subsection related to reference tracking. On one hand matrix $\boldsymbol{N}_{x_q} = (\boldsymbol{0}_3, \boldsymbol{I}_3)^T$, generates zero reference for rotational velocity, but feeds-through quaternion reference. On the other hand $\boldsymbol{N}_{x_\omega} = (\boldsymbol{I}_3, \boldsymbol{0}_3)^T$, ignores feed-through from rotational velocity reference to quaternion reference. Matrix $\boldsymbol{C} = (\boldsymbol{0}_3, \boldsymbol{I}_3)$ selects just reduced quaternion from the vector containing signals related to the rotational velocity and reduced quaternion.

5.5 Closed loop analysis

5.5.1 Integral MIMO controller

In this subsection, a designed controller from the previous section is analyzed to verify stability requirements. In this section by term reference is understood signal r_q and as output signal q. Monte Carlo analysis with high-fidelity simulation will be performed in part III.

In the analysis I will use a linear control-oriented model with flexible appendages 3.6 as system $\boldsymbol{G}$. The reason is, that it is essential to see what happens with flexibility modes, especially when perturbing system parameters.

In the figure 5.4 can be seen singular values of typical closed-loop transfer functions used in mixed sensitivity problem. This analysis is conducted on the nominal system. At first sight can be seen that flexible modes are noticeably damped, but the controller does not do anything with these modes, but these oscillations are negligible. The bandwidth of the controller is about 0.5 rad/s. It is approximately one order behind flexible modes. Interesting is, how varies the attenuation of flexible modes, when including parametric uncertainty in the range of 50% of the nominal value. From the figure 5.5 can be seen, that attenuation varies in orders, but the amplitude is smaller than one. Oscillation frequency varies too, but not very significantly.

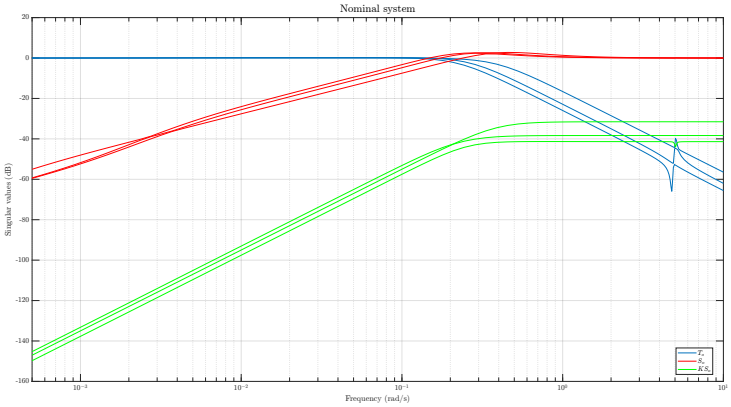

Figure 5.4: Singular values of closed-loop transfer functions with designed MIMO integral controller

Singular values of the transfer function from disturbance torque to control error are important for APE analysis. From the figure 5.6 can be seen that parametric uncertainties don't affect disturbance rejection. Using the relation 5.3 and identified data from disturbance signal analysis an estimated worst case APE value in amplitude is $APE_{\text{est}} = 150\,\text{arcsec}$, which satisfies performance requirements and will be validated in high-fidelity simulation later.

By looking at the H_∞ norm of the transfer loops from ECSS requirements, all of them meet ECSS requirements. All closed-loop systems are stable.

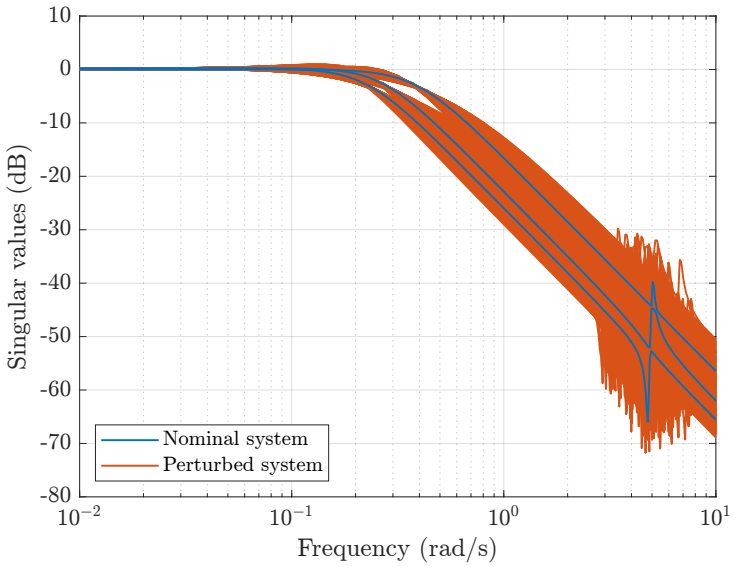

Figure 5.5: Singular values of output complementary sensitivity function with designed MIMO integral controller

Additionally, these requirements are met for parametric uncertainty in the range 50% from the nominal value in each parameter of the control-oriented model. The worst case singular values are in the table below. The same comparison was made for disk margin. The smallest gain and phase parameters of disk margins were selected. Results of this sensitivity analysis are in the table 5.1.

Measure	**Nominal system**	**Perturbed systems worst case**
$\|T_o\|_\infty$ (dB)	0.21	0.99
$\|S_o\|_\infty$ (dB)	2.78	3.38
$\|T_i\|_\infty$ (dB)	2.45	3.17
$\|S_i\|_\infty$ (dB)	0.18	0.92
Disk margin gain (dB)	3.6	3.13
Disk margin phase ($\circ$)	23.3	20.2

Table 5.1: Sensitivity analysis of stability measures to parametric uncertainty of closed-loops with designed MIMO integral controller

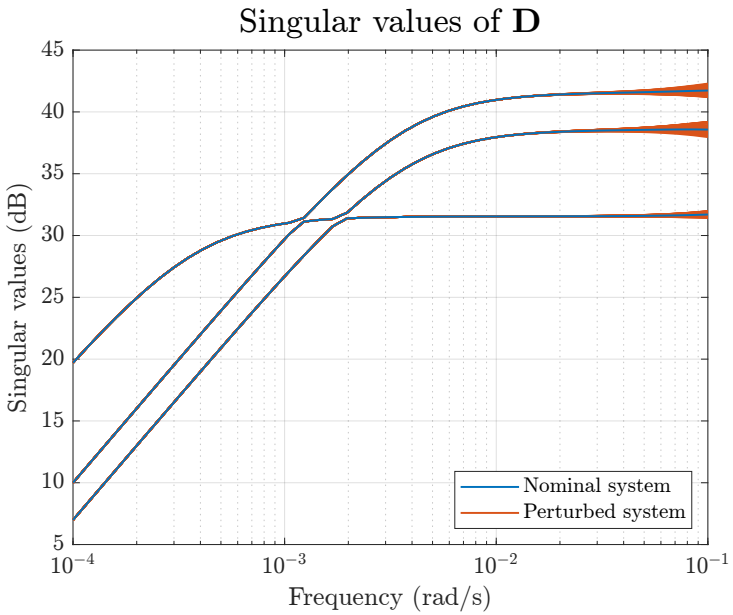

Figure 5.6: Singular values of transfer function from disturbance to control error with designed MIMO integral controller

5.5.2 Baseline SISO designed controller

Controller from subsection 3.6 is analyzed similarly as in the previous section, just $\boldsymbol{K}$ is different. As in the previous subsection, flexible modes are damped and not canceled out by the controller. The bandwidth is similar to the one from the previous section 0.5 rad/s. Flexibility modes change with parametric uncertainty similarly as for the MIMO integral design. This can be seen in the figure 5.7.

The difference between these two control strategies is in the disturbance rejection, as can be seen from figure 5.9. Integral controller damps disturbances at lower frequencies better, than the SISO controller. What have both controllers in common, that at the frequency of environment disturbances, orbit rate, and higher harmonics of it, the disturbance rejection properties do not change with changing parameters of the system.

Sensitivity analysis to parametric uncertainty was conducted at this design too. The results are given in table 5.2. This design meets the ECSS stability requirements. To comment briefly, the SISO design has slightly lower H_∞ norms than the integral MIMO design. The disk margin is slightly worse than the MIMO integral design. Disk margin difference can be explained by MIMO design when axes coupling was considered during the design of the controller.

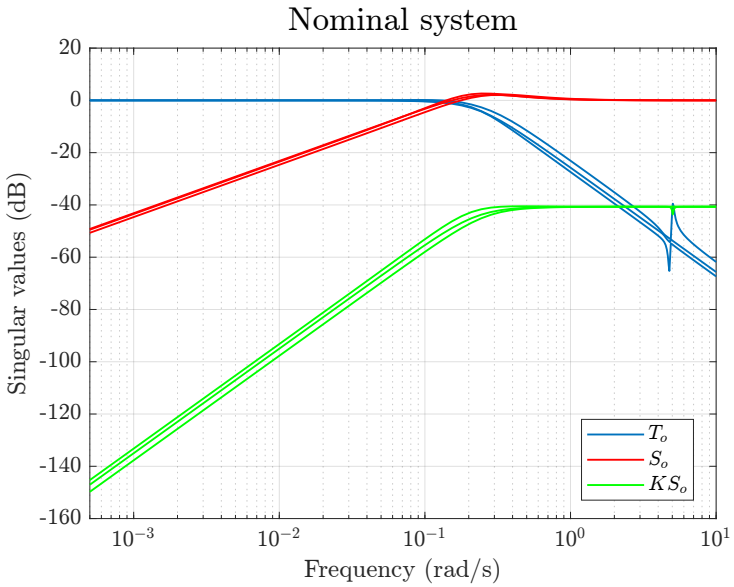

Figure 5.7: Singular values of closed-loop transfer functions with baseline SISO designed controller

Measure	Nominal system	Perturbed systems worst case
$\|T_o\|_\infty$ (dB)	0.16	0.87
$\|S_o\|_\infty$ (dB)	2.64	3.23
$\|T_i\|_\infty$ (dB)	2.41	3.03
$\|S_i\|_\infty$ (dB)	0.16	0.87
Disk margin gain (dB)	3.5	3.16
Disk margin phase ($\circ$)	22.4	20.4

Table 5.2: Sensitivity analysis of stability measures to parametric uncertainty of closed loops with baseline designed controller

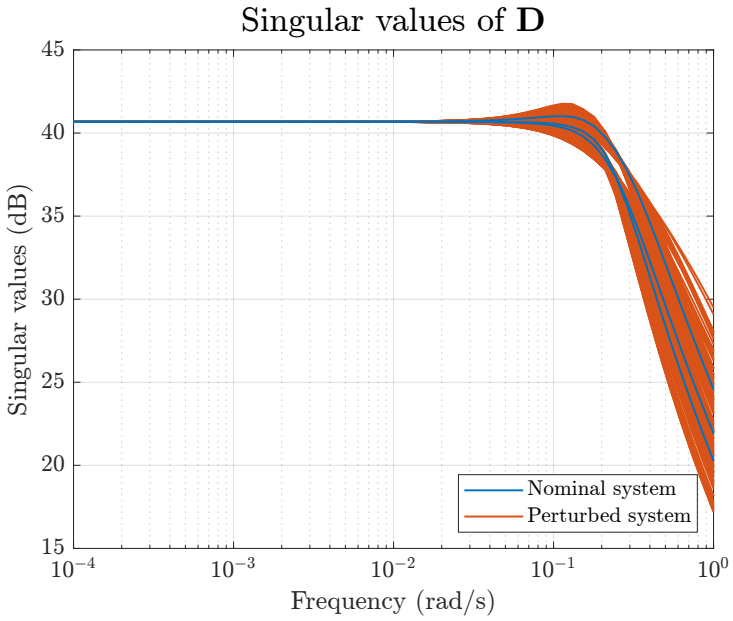

Figure 5.8: Singular values of the transfer function from disturbance to control error with baseline SISO designed controller

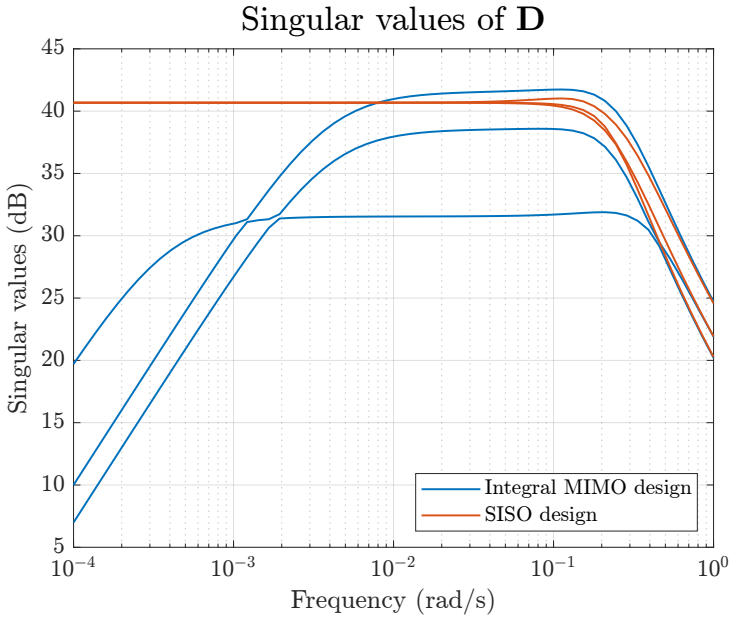

Figure 5.9: Disturbance rejection comparison of baseline and MIMO integral controller

Chapter 6

H_∞ control

A classical approach to design a controller is loop shaping, in which the magnitude of open loop transfer function L is shaped, by selecting the appropriate controller K. Usually, no optimization is needed and the designer designs $|L|$ with desired bandwidth, slopes, etc. However, it is difficult to apply this method for complex systems and other design methods should be selected. Furthermore, the final response of the closed-loop system is determined by sensitivity and complementary sensitivity transfer functions S and T, which are dependent on L. So an alternative method is to shape directly loops S and T by selecting "bounds" weights on these transfer functions. Another approach how to change the loop of the system is a signal-based approach. Instead of weighting signals in the time domain, signals are weighted in the frequency domain, which can be also formulated as H_∞ control problem [20].

In this chapter will be designed controllers using signal-based H_∞ control. The method can be better described on general control configuration, depicted in the figure 4.1b. Taking into account the general control configuration a controller K is found in order to minimize the H_∞ norm of the transfer function from w to z. This transfer function is given by the lower linear fractional transformation 6.1 [20]. For solving this problem and finding the controller K a function *hinfsyn* from Robust Control Toolbox is used [21].

$$z = F_l(P, K)w \tag{6.1}$$

6.1 Signal-based H_∞ design

In this section, a controller will be designed by signal-based H_∞ system norm minimization and analyzed. For the design of the controller a linear system, which takes into account flexible appendages 3.6 is considered. The outputs of the system are just quaternion states measured by a star tracker sensor. Taking this into consideration, the controller does not use rotational speed error. This approach may be beneficial in fine pointing mode because it does not need an angular speed measurement, which is given by onboard MEMS gyro with all its drawbacks such as drifts, sensitivity to temperature, vibrations, etc [1].

6.1.1 Obtaining a generalized plant P

To obtain a generalized plant $\boldsymbol{P}$, firstly a vector of exogenous inputs $\boldsymbol{w}$ has to be defined. In this scenario as exogenous inputs are considered reduced quaternion reference signals $\boldsymbol{r}$, disturbance torque $\boldsymbol{d}$ and measurement noise $\boldsymbol{m}$, $\boldsymbol{w} = (\boldsymbol{r}, \boldsymbol{d}, \boldsymbol{m})^T$. Exogenous outputs consists of weighted control error $\boldsymbol{e}$, weighted controller output $\boldsymbol{u}$ and weighted system output $\boldsymbol{q}$, which is reduced quaternion, $\boldsymbol{z} = (\boldsymbol{e_w}, \boldsymbol{u_w}, \boldsymbol{q_w})^T$. Additionally, control input into the generalized plant is controller output $\boldsymbol{u}$ and as the controller input $\boldsymbol{v}$ is control error $\boldsymbol{e}$.

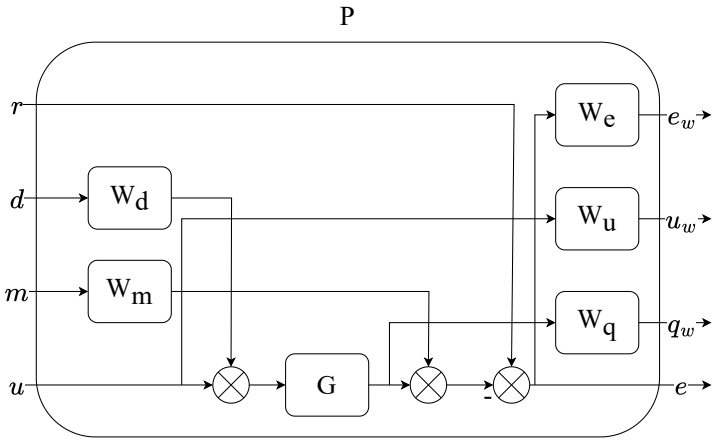

Figure 6.1: Generalized plant used in signal based approach

As can be seen from the figure 6.1, exogenous inputs and outputs are weighted. Weights were selected as polynomial 3×3 matrices with transfer functions on their diagonals. Each of the weighted signals is a vector with three elements.

W_d Input disturbance weight

Disturbance weight was designed using the knowledge about environment torques, which were analyzed in the subsection 3.7.4. I selected a weight of the third order, which increases an order of generalized plant $\boldsymbol{P}$ and of controller $\boldsymbol{K}$. This transfer function penalizes the most disturbances at the orbit rate and its higher harmonics. The weight is a matrix of transfer functions, which has the same weight W_d on diagonal and zeros at all off-diagonal elements.

$$W_d = 0.0002 \frac{(s+0.1)^2(s+10^{-7})}{(s+0.01)^2(s+10^{-4})} \tag{6.2}$$

W_m Measurement noise weight

Although the measurement noise is white noise, this noise is penalized by first order weight at frequencies of orbit rate and higher. Putting this weight

helped to attenuate RPE over one second, mostly when having disturbance at orbit rate. $\boldsymbol{W}_m$ is a diagonal transfer function matrix, with the same transfer functions on each element of diagonal W_m.

$$W_m = 0.001\frac{s+10^{-7}}{s+10^{-4}} \tag{6.3}$$

W_e Control error weight

Control error is weighted to better track signals at lower frequencies than orbit rate and better reject disturbances at lower frequencies. The same weight is used for each axis, and the $\boldsymbol{W}_e$ transfer function has all off-diagonal elements zeros.

$$W_e = 0.1\frac{s+9.95\,.10^{-4}}{s+9.95\,.10^{-8}} \tag{6.4}$$

W_u Controller output weight

This weight penalizes controller output at high frequencies. Looking from another perspective, this weight penalizes the transfer function $\boldsymbol{KS_o}$, which is known from the mixed sensitivity H_∞ control problem. This transfer function represents the relation between reference signal $\boldsymbol{r}$ and controller output $\boldsymbol{u}$, but after introducing measurement noise as input, it also represents in magnitude the transfer function from measurement noise $\boldsymbol{m}$ to control input $\boldsymbol{u}$. Analyzing the controller output from the 42 Simulator and selecting this transfer function influences how much measurement noise is in the controller output. For simplicity, each axis has the same weight, which is

$$W_u = \frac{100s+0.1}{s+10} \tag{6.5}$$

W_q System output weight

The output signal of the system is weighted with the aim, of shaping the complementary sensitivity function. The shape of the complementary sensitivity function is determined by the weight W_q. The weight was selected to achieve a reasonable H_∞ norm of closed-loop transfer functions to meet ECSS requirements.

$$W_q = 20\frac{(s+0.4)^2}{(s+3)^2} \tag{6.6}$$

6.1.2 APE requirement and W_d

The relation between disturbance and control error/APE is the same transfer function $\boldsymbol{D}$ as in the equation 5.2 for the state-space designed controller. In the figure 6.2 can be seen a relation between singular values of $\boldsymbol{D}$ and $1/\boldsymbol{W}_d$.

Using this coupling, the APE requirement APE_{req} can be directly translated into the weight design.

Assuming, that on disturbance frequencies ω_d of orbit rate and its higher harmonics a transfer function $\boldsymbol{D}$ has same maximal singular values on range of ω_d. Then from equation 5.3 maximal singular value of $\boldsymbol{D}$ can be expressed by relation 6.7. This is the benefit of signal-based H_∞ control, that by penalizing the disturbance signal $\boldsymbol{d}$, an effect of disturbance on APE can be attenuated in a way, to meet APE requirements. It is much more straightforward than tuning matrices $\boldsymbol{Q}$, $\boldsymbol{R}$, and finding the controller by solving the LQR problem.

$$\overline{\sigma}(\boldsymbol{D}(\omega_d)) = \frac{APE_{\text{req}}}{k \sum_{i=1}^{3} d(\omega_{Oi})} \tag{6.7}$$

In case, that after controller synthesis, singular values of $\boldsymbol{D}(\omega_d)$ do not meet values from equation 6.7, changing gain of filter W_d will help to meet APE requirements.

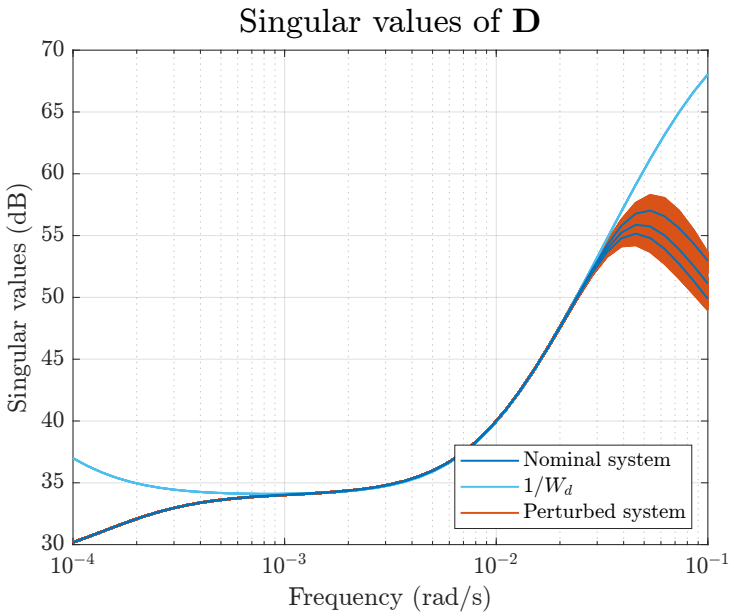

Figure 6.2: Relation of singular values of $1/\boldsymbol{W}_d$ and singular values of $\boldsymbol{D}$ of perturbed with 50% parametric uncertainty and nominal system

6.1.3 Closed loop analysis

Analysis of the closed-loop is conducted in the same way as in the section 5.5. In the figure 6.3 singular values of transfer functions used in mixed sensitivity problem are shown. After the synthesis of the controller, the controller is of order 34. By comparing to the figure 5.4 for MIMO integral controller, it can be seen that $\boldsymbol{T}_o$ ans $\boldsymbol{S}_o$ has a higher peak, resulting in higher H_∞ norm of transfer functions. When it comes to flexible appendages they are damped similarly. The significant difference is in the steepness of $\boldsymbol{S}_o$. Control input is damped at higher frequencies.

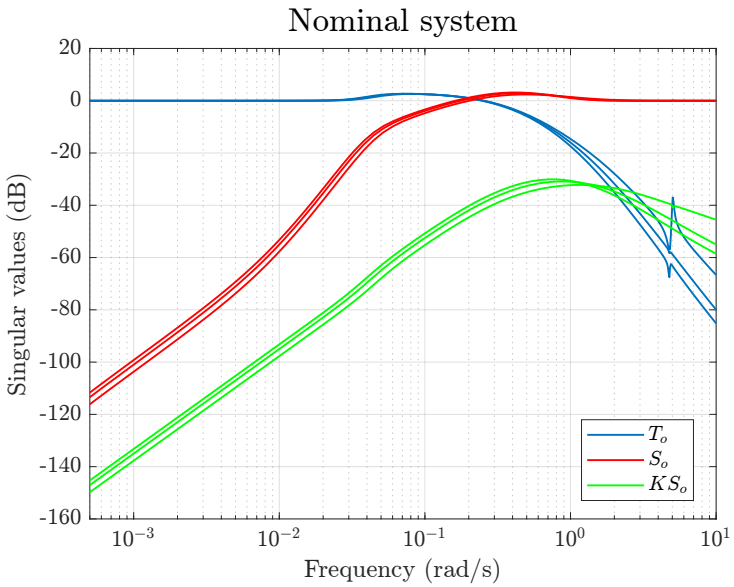

Figure 6.3: Singular values of closed-loop transfer functions with H_∞ signal based designed controller

Including parametric uncertainty into the system changed bandwidth and frequency of peaks. Additionally, flexible modes are less damped. Based on these observations system is overall more sensitive to parametric uncertainty. This is supported by the table summarizing this sensitivity analysis 6.1. The nominal system meets ECSS requirements and has a better disk margin than both controllers analyzed in the previous chapter. However, the perturbed system is more sensitive to parametric uncertainty in the scope of stability measures and does not meet ECSS requirements for the 50% range of parameter values. I explain it by a high order of the controller. In the end, the controller is some function of system and weights parameters, so this uncertainty is somehow projected in higher sensitivity. Taking into account 40% parametric uncertainty ECSS requirements are met.

Relation of APE and disturbance signal was described. Interesting is, that APE performance is not dependent on parametric uncertainty in the frequency range ω_d of disturbance $\boldsymbol{d}$. This is the same as for the state-space designed controller. The parametric uncertainty affects the influence of disturbances at higher frequencies, but as was analyzed earlier, disturbances considered in this thesis are not at these frequencies.

6.2 Fixed structure controller design

The same control problem from the subsection 6.1.1 can be solved similarly, but the function synthesizing the controller has prior knowledge about the wanted controller structure. It is the same problem as using *hinfsyn*, but there is put a constraint for controller structure in control problem formulation. For synthesizing controller with fixed structure a function *hinfstruct* from

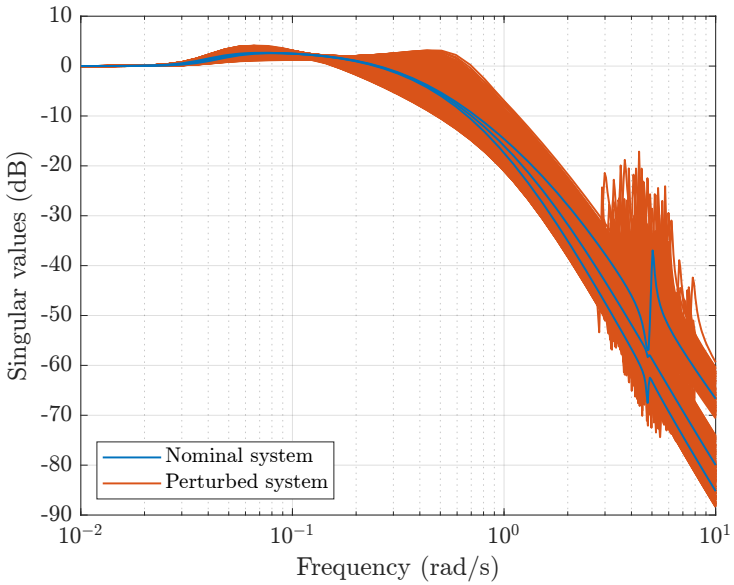

Figure 6.4: Singular values of output complementary sensitivity function of system with 50% parametric uncertainty with H_∞ signal based designed controller

Robust Control Toolbox was used [21].

I selected the controller structure of three PID controllers on diagonal. So each PID controller has on input quaternion error in i-th axis e_{qi} and outputs torque command in the same axis u_i. Matrix notation of this controller in the Laplace domain is in the relation 6.8. Additionally, I used the same weights for penalizing signals.

$$\boldsymbol{u}(s) = \begin{pmatrix} PID_x & 0 & 0 \\ 0 & PID_y & 0 \\ 0 & 0 & PID_z \end{pmatrix} \boldsymbol{e}_q(s) \tag{6.8}$$

After solving the control problem, I conducted the same analysis as in the section 6.1.3. The shape of $\boldsymbol{D}$ is changed, which results in better APE. This can be said based on the plot of singular values of $\boldsymbol{D}$ in the figure 6.5. This approach has also a disadvantage, that for the type of weight $\boldsymbol{W}_d$ from section 6.1 it is not easy to achieve specific APE directly, but weight has to be tuned. Because achieved APE is better, it can cause worse stability measures. One option is to directly change the shape of the weight. Another way is to adjust the gain until wanted APE/singular values of $\boldsymbol{D}$ are achieved.

Better disturbance rejection an APE has a disadvantage in higher H_∞ norms of closed-loop transfer functions, which for the perturbed system does not meet ECSS requirements. Also, there is a change in some closed-loop transfer functions used in mixed sensitivity problem in comparison with the controller of order 34. The advantage of this controller is, that its order is 6.

Measure	**Nominal system**	**Perturbed systems** 50% **worst case**	**Perturbed systems** 40% **worst case**
$\|T_o\|_\infty$ (dB)	2.67	4.34	3.90
$\|S_o\|_\infty$ (dB)	3.16	6.09	5.00
$\|T_i\|_\infty$ (dB)	2.67	4.34	3.90
$\|S_i\|_\infty$ (dB)	3.16	6.09	5.00
Disk margin gain (dB)	4.0	2.63	3.09
Disk margin phase ($\circ$)	25.9	17.1	19.99

Table 6.1: Sensitivity analysis of stability measures to parametric uncertainty of closed loops with signal based H_∞ designed controller

Measure	**Nominal system**	**Perturbed systems** 50% **worst case**	**Perturbed systems** 40% **worst case**
$\|T_o\|_\infty$ (dB)	4.94	7.28	6.87
$\|S_o\|_\infty$ (dB)	5.04	7.07	6.48
$\|T_i\|_\infty$ (dB)	4.94	7.28	6.87
$\|S_i\|_\infty$ (dB)	5.04	7.07	6.48
Disk margin gain (dB)	2.75	2.1	2.28
Disk margin phase ($\circ$)	17.9	13.7	14.86

Table 6.2: Sensitivity analysis of stability measures to parametric uncertainty of closed loops with signal base H_∞ fixed structure designed controller

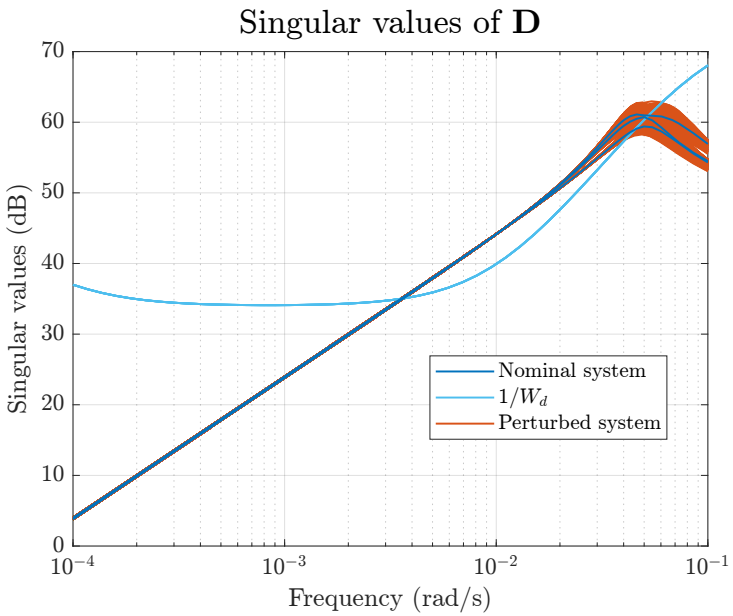

Figure 6.5: Relation of singular values of $1/\boldsymbol{W}_d$ and singular values of $\boldsymbol{D}$ of perturbed with 50% parametric uncertainty and nominal system for fixed structure designed controller

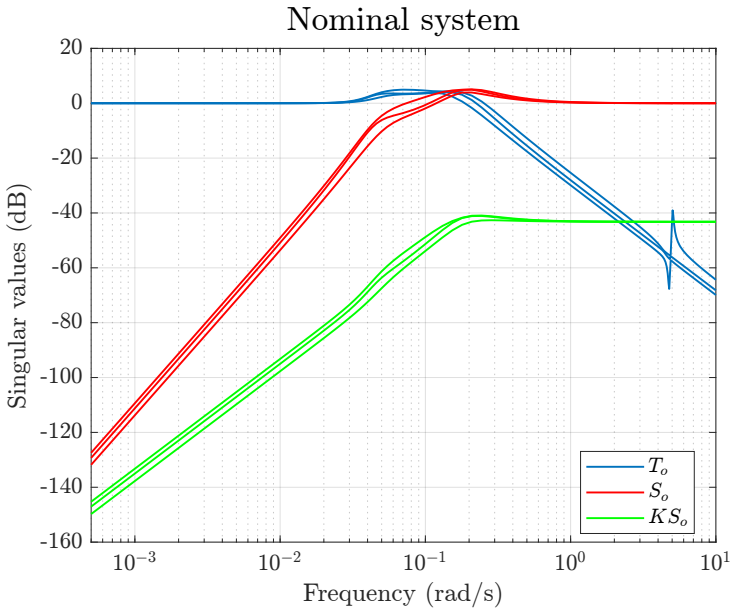

Figure 6.6: Singular values of closed-loop transfer functions with H_∞ signal based fixed structure designed controller

Part III

Controllers validation

Chapter 7

Software in the loop simulations

In this chapter feedback control laws designed in the previous part are validated in high-fidelity simulator 42 with all other flight software components. For clarity and simplicity of notation in the analyses, controllers are labeled as follows

- $\boldsymbol{K}_0$ stands for baseline controller described in 3.6.
- $\boldsymbol{K}_1$ stands for MIMO integral controller designed in subsection 5.4.
- $\boldsymbol{K}_2$ stands for H_∞ designed controller using *hinfsyn* function on generalized plant from section 6.1.1.
- $\boldsymbol{K}_3$ stands for H_∞ designed controller using *hinfstruct* function on generalized plant from section 6.1.1 with a PID controller for each axis.

7.1 Controller implementation

The feedback control law is in the flight software defined as a function, with a fixed number of inputs and outputs. A control error vector is fed into the controller and the controller function outputs three torques. Simply, the controller is a system with control error on input and control action on output. The designed controllers are dynamic with multiple states, so just one matrix multiplication is not enough. The designed controllers in MATLAB are augmented by zeros, if needed, to meet input of the function requirements. Especially H_∞ designed controllers use just quaternion errors, so by augmenting the controller by zeros, input dimensions are satisfied, and rotational speed control error is not propagated further. After augmenting, the controller is discretized and rewritten into state space representation. After that, it is just matrix multiplication, of evaluation of a discrete state space model using controller state and controller input.

7.2 Fine pointing mode

In mode satellite shall hold the same attitude, for example in the orbital frame holding the nadir attitude means that the satellite looks with its camera at Earth. This is needed for Earth observation and this scenario will be validated in this section. Holding attitude in the inertial coordinate frame is used for telescopes when they are pointed to specific part of the sky, stars, planets, etc... For fine pointing from a mission perspective is important to have low APE and RPE, especially for telescopes, where a long exposition is needed and the image can not be blurred. Additionally from a control perspective knowledge about control error is an interesting measure, which is for small angles in the form of APE. Important is the controller output too, which will be validated in this section. Important is to note, that feedforward is not used, because in this mode it does not have any effect.

Looking at the figure A.1 it can be seen that in the scope of RPE, controllers behave similarly. The difference is in the noise modulated on the control signal. The worst in this category is controller $\boldsymbol{K}_1$. The biggest differences are in the APE performance measure, where SISO designed controller $\boldsymbol{K}_0$ has the highest APE in all axes. Additionally when comparing linear sensitivity analyses of controllers $\boldsymbol{K}_0$ and $\boldsymbol{K}_1$, from tables 5.2, 5.1 can be seen, that they have similar singular values of closed-loop transfer functions, mentioned in the ECSS as stability measures, but performance differs.

In the SIL simulation best performs the controller $\boldsymbol{K}_3$, in terms of APE, RPE and control command. Unfortunately, this controller does not meet ECSS requirements when perturbed. Between state-space designs and $\boldsymbol{K}_3$ in terms of APE and control action is the controller $\boldsymbol{K}_2$.

It has to be mentioned that these controllers do not use any information about the rotational velocity of the satellite and in terms of APE and noise of control signal they are better than $\boldsymbol{K}_1$, additionally their tuning is easier.

The same analysis was conducted for the spacecraft holding attitude in inertial frame, reduced quaternion reference $\boldsymbol{r}_q = (0, 0, 0)^T$. The problem with simulating in the high-fidelity simulator as 42 is, that a star tracker sensor used in fine pointing mode is not available(blinded or looks at Earth) at some parts of orbit, so it can't hold attitude all the time as in nadir pointing. But in the parts of the orbit where a star tracker was available, it has a similar performance as for nadir pointing. Especially RPE is smaller. The standard variation of noise modulated on controller output is the same as in the nadir case.

Another important thing is that these high-fidelity simulations confirmed the results of the linear analysis. The relation 5.3 for estimating worst case APE from knowledge about singular values of $\boldsymbol{D}$ and frequency characteristic of disturbance signal is correct. This knowledge is very important for the formulation of generalized plant $\boldsymbol{P}$ in H_∞ control problem, while designing filter $\boldsymbol{W}_u$ because formula 6.7 can be used.

	max(APE) (arcsec) / axis		σ(RPE) (arcsec) / axis		Control signal noise σ (μNm) / axis	
C	Nadir	Inertial	Nadir	Inertial	Nadir	Inertial
$\boldsymbol{K}_0$	356 / x	395 / y	2.5 / x	1.0 / z	1.7 / z	1.7 / z
$\boldsymbol{K}_1$	151 / x	184 / z	2.57 / x	1.0 / z	2.17 / x	2.17 / x
$\boldsymbol{K}_2$	193 / x	188 / y	2.45 / x	1.5 / z	1.5 / z	1.4 / z
$\boldsymbol{K}_3$	115 / x	167 / z	2.43 / x	0.84 / z	1.0 / z	1.0 / z

Table 7.1: Comparison of designed controllers and baseline controller in fine pointing scenarios

7.2.1 Monte Carlo simulations

In the Monte Carlo simulation, I perturbed parameters as it is recommended, see subsection 4.2.3. For better work with data, just one orbit is simulated instead of three. The main criteria for this analysis is to confirm theoretical results from linear analysis and this is, that all systems are stable and APE is not affected by parametric uncertainty. For the Monte Carlo campaign, I ran 200 simulations, which sample all 15 parameters of the system 3.5. The campaign is run in the 42 nonlinear simulator with a satellite model.

Behaviour of system with integral MIMO controller is in the figure A.3, parametric uncertainty does not affect the system. This confirms the linear analysis conducted in the section 5.5, where from the plot of singular values of transfer function $\boldsymbol{D}$, can be seen that singular values are not affected in the frequency of disturbance signal. From tables 7.2, 7.3 can be seen, that same is valid for the other controllers, as linear analysis shown. An absolute error $e_x = x_p - x_n$, where x_p stands for perturbed system signal and x_n for nominal system signal is defined.

From the table related to the APE can be seen that in inertial pointing performance worsens much more with parametric uncertainty than in nadir pointing. But these errors are caused by phase shift, no change in amplitude. But looking at the table for control input u, it can be observed a slighter increase in controller output for all other controllers except $\boldsymbol{K}_1$.

	APE Analysis			
	Nadir		Inertial	
C	max(e_{APE}) (arcsec)/axis	$\sigma(e_{APE})$ (arcsec)/axis	max(e_{APE}) (arcsec)/axis	$\sigma(e_{APE})$ (arcsec)/axis
$\boldsymbol{K}_0$	6.2/z	1.5/y	38.9/z	12.0/z
$\boldsymbol{K}_1$	6.8/z	1.7/z	7.4/z	1.72/z
$\boldsymbol{K}_2$	12.6/z	3.8/z	51.8/z	17.3/z
$\boldsymbol{K}_3$	15.3/z	4.8/z	52.8/z	16.9/z

Table 7.2: Comparison of Monte Carlo simulations of designed controllers and baseline controller in fine pointing scenario for APE measure

Concluding the analysis of this section, all controllers in the fine pointing

	Controller output analysis			
	Nadir		Inertial	
C	max(e_u) (μNm)/axis	$\sigma(e_u)$ (μNm)/axis	max(e_u) (μNm)/axis	$\sigma(e_u)$ (μNm)/axis
$\boldsymbol{K}_0$	1.7/z	0.5/z	10.2/z	2.1/z
$\boldsymbol{K}_1$	1.8/x	0.5/x	1.8/x	0.6/x
$\boldsymbol{K}_2$	0.4/z	0.1/z	9.2/z	2.0/z
$\boldsymbol{K}_3$	0.2/z	0.1/z	6.6/z	1.48/z

Table 7.3: Comparison of Monte Carlo simulations of designed controllers and baseline controller in the fine pointing scenario for controller output measure

mode meet the mission requirements. The worst indicators were mostly identified in the z axis. This can be explained by star tracker mounting. In the z axis has star tracker has the highest measurement noise and noise propagates through the system. Additionally, the correctness of linear analysis was verified by these high-fidelity simulations with parametric uncertainty and the formulas related to APE are correct.

7.3 Object tracking mode

In this section feedback control laws designed in the previous part are validated in nonlinear attitude simulator 42 with all other flight software components, mostly guidance affects object tracking by computing reference signals for controllers. During the maneuver star tracker sensor can not be used(the guidance algorithm does not include pointing constraints on the star tracker). This can be seen in the figure 7.1, where the white cone represents a field of view of the star tracker and points to the Earth. The green pyramid represents the field of view of the camera. For comparison of controllers in feedback is used ground-truth attitude instead of measurement from sensors, to demonstrate the tracking capabilities of controllers. Two scenarios when feedforward is enabled and disabled are evaluated.

In the figure A.2 can be seen that the satellite performs maneuver in changing attitude from nadir attitude to the attitude pointing to the object, whose location is Lat = 16.01°, Lng = −16.24° and zero altitude above sea level, which are coordinates of Dakar. The maneuver is performed from 1600s to 1700s in simulation time. As can be seen, the H_∞ designed controllers $\boldsymbol{K}_2$, $\boldsymbol{K}_3$ have bad transient properties, even in case, that feedforward is enabled. The best performs $\boldsymbol{K}_1$ controller. Additionally, each of the controllers saturates the input of the system, which does not help transient properties. The maneuver is shown in the plot to show, how controllers behave while the satellite is changing its attitude.

The maneuver of re-orienting is not part of object tracking, so in table 7.4 the data from the 1850s will be analyzed and compared, to see how controllers deal with object tracking.

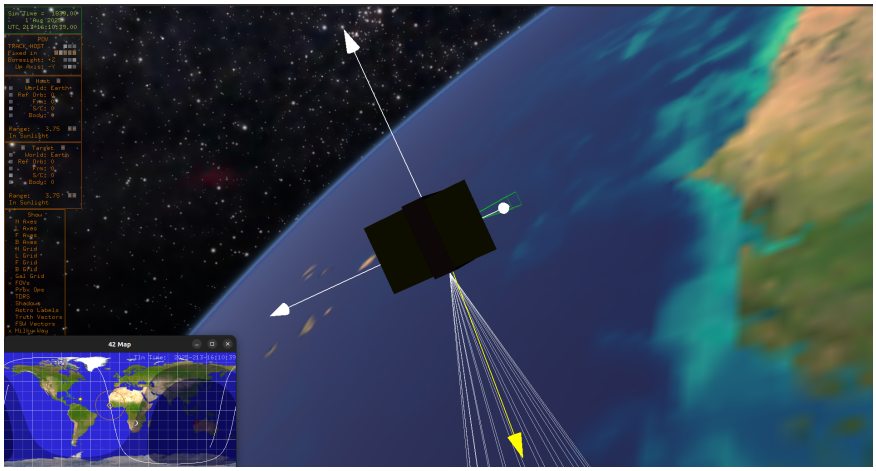

Figure 7.1: Screenshot from 42 simulator showing satellite during Dakar tracking

	max APE (arcsec) / axis / time(s)		Control signal noise σ (μNm) / axis	
C	No FF	With FF	No FF	With FF
$\boldsymbol{K}_0$	813/y/2006	350/y/1996	7.1/y	27.3/x
$\boldsymbol{K}_1$	774/y/2000	379/y/1995	7.1/y	28.8/x
$\boldsymbol{K}_2$	2895/y/1990	928/y/1982	7.3/y	25.0/x
$\boldsymbol{K}_3$	4877/x/1989	1570/y/1982	7.7/y	25.0/x

Table 7.4: Comparison of designed controllers and baseline controller in the fine pointing scenario from simulation time 1850s

From the figure A.2 can be seen in APE, that H_∞ designed controllers are not tuned for this simulation case, they oscillate. With enabled feedforward, all controllers meet the mission requirements for APE. RPE is not validated, because of missing measurement noise. Interesting is, that the controller output is noisy with feedforward enabled. I explain it by an error in the implementation of the guidance algorithm or numeric instability of computations in the guidance subsystem. Good is, that this noisy control input is not saturated, so the satellite can work in its operational range. Without enabled feedforward just the controllers $\boldsymbol{K}_0$ and $\boldsymbol{K}_1$ meet mission requirements for APE.

7.3.1 Monte Carlo simulations

In the Monte Carlo simulation of the object tracking scenario, the same parameters and in the same range are perturbed as for fine pointing case. It can be seen that without feedforward just two controllers can be compared, so Monte Carlo simulations were run just with feedforward enabled. The same measures were evaluated. From the table 7.5 can't be seen directly if for all cases controllers meet mission requirements. For $\boldsymbol{K}_2$, the maximum APE is 2000 arcsec, which does not meet the requirement for about 200

arcsec. This can be solved by tuning, lowering the penalization of disturbance, and attenuating disturbance rejection. The controller $\boldsymbol{K}_3$ does not meet the mission requirements when perturbed. Interesting is, computing the maximum relative error. For all controllers relative error caused by parametric uncertainty is around 33%. After this analysis, just controller $\boldsymbol{K}_0$ and $\boldsymbol{K}_1$ meets the mission APE requirements for object tracking.

	Object tracking analysis			
	e_{APE}		e_u	
C	$\max(e_{APE})$ (arcsec)/axis	$\sigma(e_{APE})$ (arcsec)/axis	$\max(e_u)$ (μNm)/axis	$\sigma(e_u)$ (μNm)/axis
$\boldsymbol{K}_0$	274/y	99.6/y	6.9/y	2.2/y
$\boldsymbol{K}_1$	250/y	80.3/y	7.2/y	2.4/y
$\boldsymbol{K}_2$	969/y	312.2/y	7.7/y	2.4/y
$\boldsymbol{K}_3$	1643/y	702.5/y	9.3/y	2.9/y

Table 7.5: Comparison of Monte Carlo simulations of designed controllers and baseline controller in fine pointing scenario for APE measure

7.4 Summary

To sum up, high-fidelity simulations of two scenarios from the perspective of satellite operations were conducted. Firstly, in fine pointing mode, all controllers satisfied mission requirements for fine pointing in orbital and inertial coordinate frames, with parametric uncertainty too. Additionally, the linear analysis was verified by nonlinear simulation, regarding the disturbance rejection and parametric uncertainty.

Additionally, the controllers were validated in the object tracking scenario. I observed, that controllers are not good at re-orienting or changing their attitude. The transients were oscillatory, inputs were saturated. This behavior is not acceptable for the H_∞ designed controllers. In the object tracking scenario after transient, the responses were oscillatory for H_∞ designed controllers, but with feedforward, all met the mission APE requirements. Adding parametric uncertainty shows, that controllers $\boldsymbol{K}_2$, $\boldsymbol{K}_3$ did not meet APE requirement with perturbed systems. Adding feedforward introduces noise at the control signal. This needs further investigation to find the source of this noise. One candidate is wrongly implemented guidance for object tracking.

Comparing both situations, using the control methods shown in this thesis, I was able to find such controllers, that perform better, than the baseline SISO designed controller. The advantage of designing a controller for the MIMO system in this case was not very dominant, because of small coupling through moment of inertia matrix $\boldsymbol{J}_B$. But using proposed methods, especially H_∞ design enabled me to design SISO control law $\boldsymbol{K}_3$ but taking into account coupling between axes and controllers interference.

Firstly I tried to design using H_∞ three SISO control laws independently for each axis. Each closed-loop SISO system was stable, but after analyzing them in linear analysis on the MIMO system, closed-loop functions were unstable. The 42 simulator confirmed the linear analysis.

Another advantage is that direct APE requirement in fine pointing mode can be translated into the weight on the disturbance signal. Additionally, using H_∞ framework enables to transfer some bad properties into another axis, which is not important [20]. This was not done in this thesis.

Chapter 8

Results

In this diploma thesis, I became familiar with the dynamics and kinematics of satellite attitude in low Earth orbit. At the same time, I became familiar with the disturbances affecting the orientation of the satellite. This is described in the chapter 2.

In the chapter 3 I ran simulator 42 with a 6U CubeSat model with deployable solar panels, which I modeled and showed that flexibility and nonlinearity can be replaced by a linear model for this case. I developed control-oriented models and verified them with 42 simulator. These models were later used to design controllers. In addition, I created a frequency model of environmental disturbances affecting the satellite using data from simulator 42.

In part II I familiarized myself with ECSS standards for control systems and mission requirements for monitoring the ground, sky, and objects on Earth. Subsequently, I used the LQR optimal control method to find the integral control law. Using the H_∞ method of controller design, I designed controllers for fine pointing and object tracking. I managed to use the H_∞ methodology to translate the performance requirement for APE directly into the controller design. Using linear analysis, I analyzed and compared designed controllers, regarding the ECSS and parametric uncertainty.

At the end in part III, I verified the functionality of the controllers in SIL simulation using 42 simulator. I also verified the controllers regarding the parametric uncertainty of the system and subsequently tested them for fine pointing and object tracking.

8.1 Future work

SIL simulation showed that the controllers do not behave appropriately during re-orientation. They saturate the input, have overshoot, and oscillate. This transition is called slew mode in AOCS terminology. Normally, another controller is designed for slew mode and then is the controller switched to fine pointing controller after maneuver. My next job would be to solve the slew mode for this satellite. It is proposed to put an MPC reference governor above the controller for fine pointing, which is good at disturbance rejection,

which would be in charge of transitions and actuators. This would avoid switching regulators and give the designer the ability to put for example pointing constraints to not lose the star tracker fix during maneuver. For this, it is necessary to expand the dynamical model with the dynamics of reaction wheels and momentum management.

Although I managed to find a relationship between the requested APE and the disturbance signal filter. I haven't looked into RPE that much, and my next job would be to find a relationship so that specific RPE and APE can be achieved by minimizing the augmented system norm. This would simplify the design of controllers satisfying mission requirements.

Chapter 9

Conclusion

In this work, a 6U CubeSat with deployable solar panels and its attitude dynamics and kinematics were presented. In short, its subsystems related to the precise attitude control of the satellite were described. By using a high-fidelity simulator, the work of creating a model of environmental disturbances and a satellite with solar panels was facilitated, which helped in the design of the controllers.

The controller design methods were described and the controllers were analyyed with the help of linear analysis, whether they meet the ECSS requirements. This work describes how to design controllers to eliminate environmental disturbances to meet APE mission requirements. In addition, parametric uncertainty was taken into account in analysis.

The controllers were designed in such a way to be implementable into the flight software of the satellite. Additionally, SIL simulations in NASA developed and used simulator 42 were conducted to verify the stability and performance of the controllers. The outcomes of a linear analysis were confirmed, by these high-fidelity simulations.

To sum up, in this thesis all steps have been taken to enable designed controllers, which satisfy requirements, to be tested in orbit, in case the satellite will be launched into space.

Bibliography

[1] F. L. Markley and J. Crassidis, *Fundamentals of Spacecraft Attitude Determination and Control*. Springer New York, 2014.

[2] ISISPACE, "iMTQ Magnetorquer Board." URL: `https://www.isispace.nl/product/isis-magnetorquer-board/`, 2024. Cited (18.05.2024).

[3] Sodern, "Sodern AURIGA-CP." URL: `https://sodern.com/wp-content/uploads/2023/12/2022-02-OnePager-Auriga-CP-v2.pdf`, 2022. Cited (18.05.2024).

[4] M. Knapp, S. Seager, B.-O. Demory, A. Krishnamurthy, M. W. Smith, C. M. Pong, V. P. Bailey, A. Donner, P. D. Pasquale, B. Campuzano, C. Smith, J. Luu, A. Babuscia, R. L. Bocchino, Jr., J. Loveland, C. Colley, T. Gedenk, T. Kulkarni, K. Hughes, M. White, J. Krajewski, and L. Fesq, "Demonstrating High-precision Photometry with a CubeSat: ASTERIA Observations of 55 Cancri e," *The Astronomical Journal*, vol. 160, p. 23, June 2020.

[5] VZLÚ, "VZLUSAT-1 has burned up in the atmosphere." URL: `http://vzlusat1.cz/en/vzlusat-1-has-burned-up-in-the-atmosphere/47/a/`, 2023. Cited (18.05.2024).

[6] VZLÚ, "QUVIK – THE FIRST CZECH SPACE TELESCOPE." URL: `https://quvik.cz/en/quvik-the-first-czech-space-telescope/`, 2023. Cited (18.05.2024).

[7] Y. Yang, *Spacecraft Modeling, Attitude Determination, and Control Quaternion-based Approach*. CRC Press, 2019.

[8] C. J. Allard, M. Diaz Ramos, H. Schaub, and S. Piggott, "Spacecraft dynamics integrating hinged solar panels and lumped-mass fuel slosh model," in *AIAA/AAS Astrodynamics Specialist Conference*, 2016.

[9] E. Stoneking, "42: A general-purpose spacecraft simulation," 2022.

[10] N. Nguyen and I. Tuzcu, "Flight dynamics of flexible aircraft with aeroelastic and inertial force interactions," in *AIAA Atmospheric Flight Mechanics Conference*, 2012.

[11] P. Valentin, J. Cieslak, D. Henry, S. Bennani, and A. Falcoz, "Robust microvibration mitigation and pointing performance analysis for high stability spacecraft," *International Journal of Robust and Nonlinear Control*, 10 2018.

[12] A. Kron, A. St-Amour, and J. de Lafontaine, "Four Reaction Wheels Management:Algorithms Trade-Off and Tuning Drivers for the PROBA-3 Mission," *The International Federation of Automatic Control*, 2014.

[13] F. Camillo, P.J.; Markley, "Orbit-averaged behavior of magnetic control laws for momentum unloading," *Journal of Guidance, Control, and Dynamics*, vol. 3, no. 6, 1980.

[14] M. Elgersma, G. Stein, M. Jackson, and J. Yeichner, "Robust controllers for space station momentum management," in *Proceedings of the 30th IEEE Conference on Decision and Control*, pp. 2206–2212 vol.3, 1991.

[15] C. M. Pong, *High-precision pointing and attitude estimation and control algorithms for hardware-constrained spacecraft*. PhD thesis, Massachusetts Institute of Technology. Department of Aeronautics and Astronautics., 2014.

[16] European Cooperation for Space Standardization, "ECSS-E-HB-60-10A - Control performance guidelines," 2010.

[17] G. F. Franklin, J. D. Powell, and A. Emami-Naeini, *Feedback control of dynamic systems*. New York: Pearson, global;eight; ed., 2014.

[18] P. Seiler, A. Packard, and P. Gahinet, "An introduction to disk margins [lecture notes]," 2020.

[19] D. Liberzon, *Calculus of Variations and Optimal Control Theory - A Concise Introduction Instructors Manual*. Princeton University Press, 2012.

[20] S. Skogestad and I. Postlethwaite, *Multivariable Feedback Control: Analysis and Design*. Chichester: John Wiley Sons, 1. ed., 1996.

[21] The MathWorks Inc., "Robust Control Toolbox," 2022.

Appendices

Appendix A

SIL simulations graphs

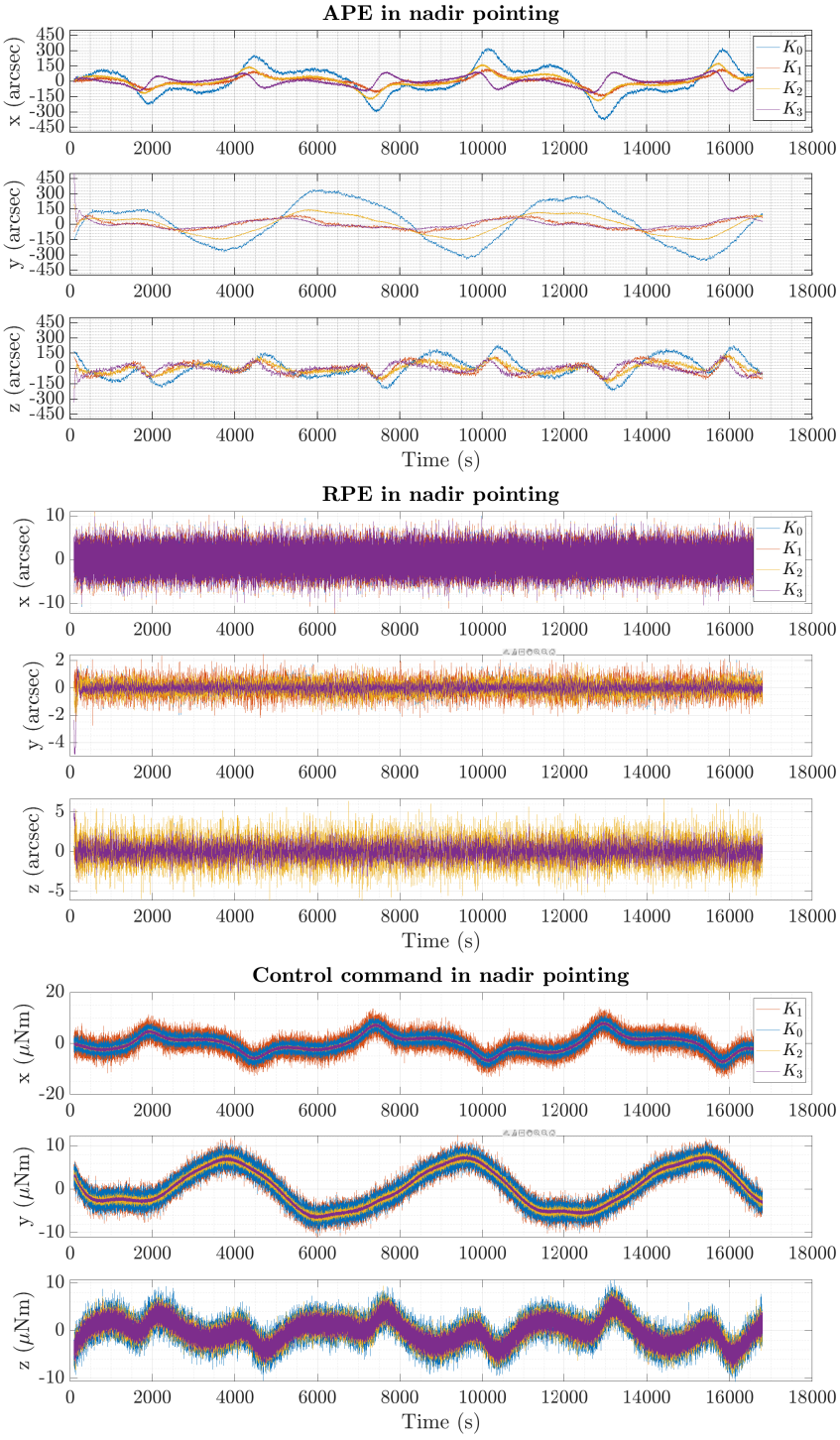

Figure A.1: Comparison of controllers in fine pointing scenario holding nadir attitude in SIL simulation

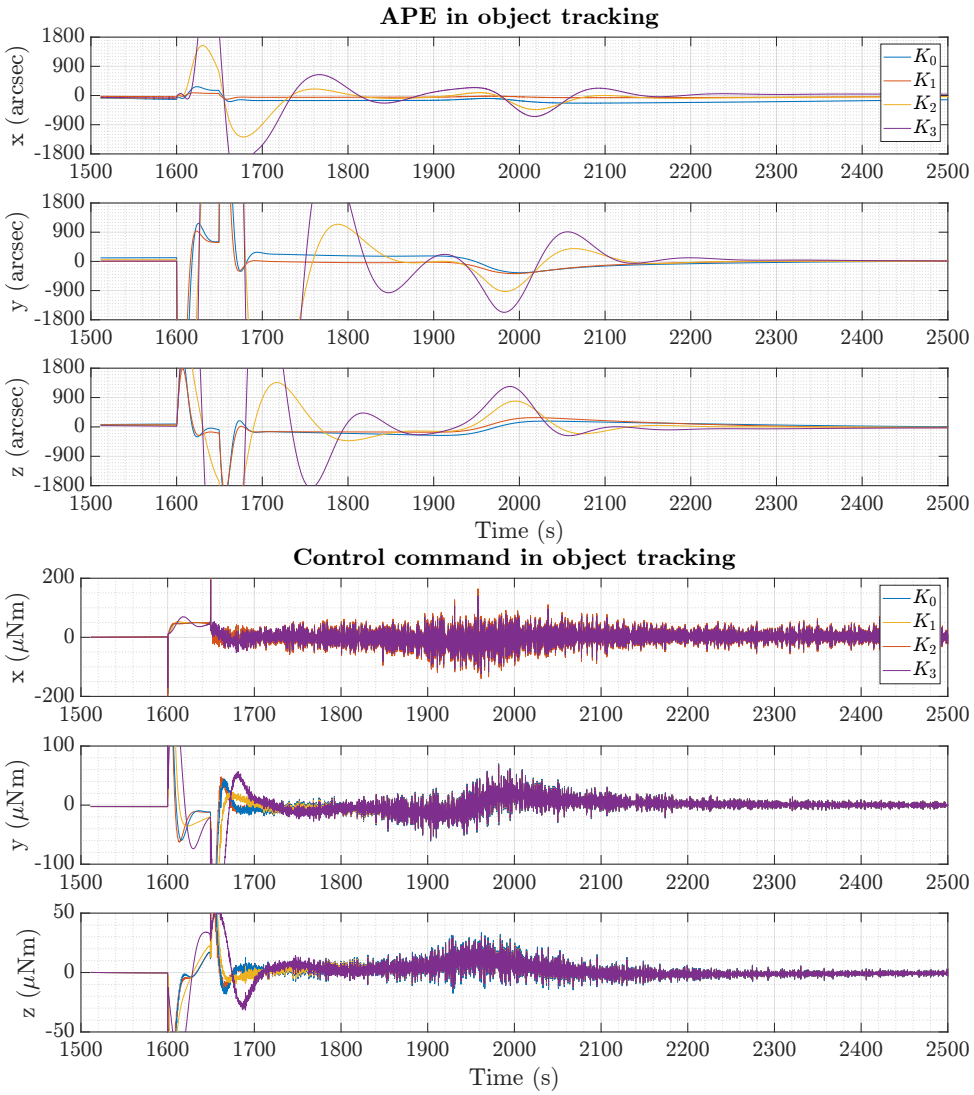

Figure A.2: Comparison of controllers in object tracking scenario with enabled feed forward in SIL simulation

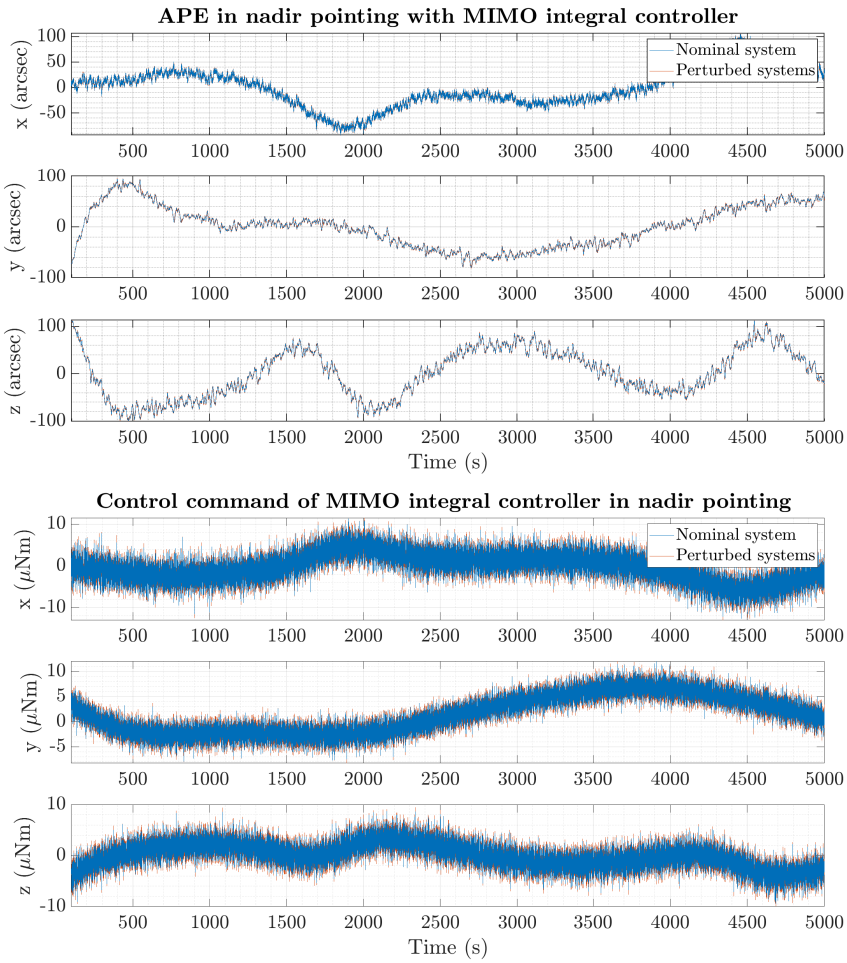

Figure A.3: Monte Carlo simulation of MIMO integral controller in fine pointing scenario holding nadir attitude

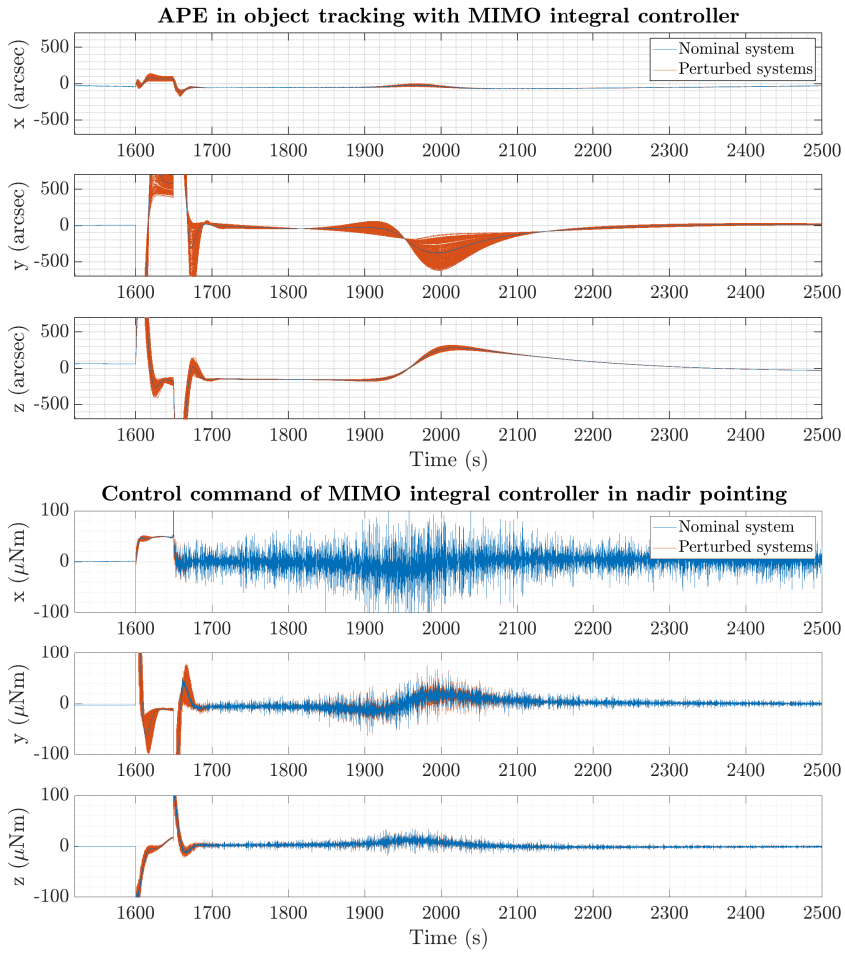

Figure A.4: Monte Carlo simulation of MIMO integral controller in object tracking scenario